Solid Earth Discuss., doi:10.5194/se-2017-44, 2017
Manuscript under review for journal Solid Earth
Discussion started: 19 May 2017

Solid Earth Discussions

Texture analysis of experimentally deformed Black Hills Quartzite

Rüdiger Kilian[1*], Renée Heilbronner[1,2]

(1) Department of Environmental Sciences, University Basel, Basel, Switzerland

(2) Department of Geology, University of Tromso, Tromso, Norway

* ruediger.kilian@unibas.ch

Abstract

The textures of three samples of Black Hills quartzite (BHQ) deformed experimentally in the dislocation creep regime 1, 2 and 3 (according to Hirth and Tullis, 1992) have been analysed by EBSD. All samples were deformed to relatively high strain, within a temperature range of 65° and identical displacement rates and are almost entirely composed of dynamically recrystallized grains.

A texture transition from peripheral c-axes in regime 1 to a central c-axis maximum in regime 3 is observed. Separate pole figures are calculated for different grain sizes, aspect ratios and long axis trend (θ) of grains, and high and low levels of intragranular deformation intensity as measured by the grain kernel average misorientation (gKAM). Misorientation relations are analysed for different texture components (named Y- B- R- and σ, with reference to previously published 'prism', 'basal', 'rhomb' and 'σ1' – grains).

Results show that regime 1 and 3 correspond to clear end member textures with regime 2 being transitional. Texture strength and the development of a central c-axis maximum from a girdle distribution depends on deformation intensity at the grain scale and on the contribution of dislocation creep which increases towards regime 3. Combined with calculations of resolved shear stresses and misorientation analysis, it becomes clear that the peripheral c-axis maximum in regime 1 is not due to deformation by basal - <a> slip. We interpret the texture transition as a result of different texture forming processes, one being more efficient at high stresses (formation of grains with peripheral c-axes), the other depending on strain (dislocation glide involving prism and rhomb slip systems), and not as a result of a temperature dependent activity of different slip systems.

Keywords:

Quartz texture, crystallographic preferred orientation, texture transition, slip systems, dislocation creep

1. Introduction

Quartz textures, usually presented in the form of pole figures are used frequently for the analysis of deformed rocks. Interpretations based on pole figures or EBSD data are widely used to make inferences about deformation kinematics such as shear senses (e.g. Berthe et al., 1979, Simpson, 1980; Kilian et al., 2011b), vorticity (e.g. Wallis, 1995; Xypolias, 2009) and progressive strain type (e.g. Price, 1985; Sullivan & Beane, 2010), deformation mechanism (Behrmann & Mainprice, 1987; Song & Ree, 2007; Kilian et al., 2011a) or recrystallization processes (e.g. Knipe & Law, 1987; Stipp et al. ,2002), involved slip systems (e.g. Bouchez & Pecher, 1981; Schmid & Casey, 1986; Law et al., 1990) or synkinematic temperature (e.g. Kruhl, 1998; Morgan & Law, 2004; Thigpen et al., 2010). However, in some cases, the underlying mechanisms and processes are poorly understood and dependencies, e.g. of temperature and recrystallization mechanisms (e.g. Stipp et al., 2002), or texture geometry and strain in polycrystalline materials are not always easily separated (e.g. Schmid & Casey, 1986; Wenk & Christie, 1991). Transitions in texture types have been correlated with (changing) recrystallization mechanisms or were explained by a temperature dependence of the slip systems involved in crystal plastic deformation (e.g. Tullis et al., 1973). There have been speculations on a temperature dependence of slip systems, either caused by a temperature dependent critical resolved shear stress during glide (Hobbs, 1985) or anisotropic diffusion during climb (e.g. Blacic, 1975), however, conclusive evidences have only been found for a transition from <a> to <c> burgers vectors towards very high temperatures (e.g. Mainprice et al., 1986). For <a>-slip, a temperature dependent activation of different slip systems has not been convincingly demonstrated. A bulk strain dependency of texture is recognized in experiment and nature (e.g. Heilbronner & Tullis, 2006; Pennacchioni et al., 2010), however, it is not too clear in which way bulk strain relates to strain at a grain scale in a deforming aggregate.

In this contribution we will focus on the following questions: Which factors influence the texture geometry (shape of pole figure skeletons)? Is the texture controlled by deformation temperature, geometry/kinematics or recrystallization processes? How reliably can certain texture components be used to infer the activity of a specific slip system? To this end, EBSD data obtained from Black Hills Quartzite (original samples of Heilbronner & Tullis 2002 and 2006) experimentally deformed in the three dislocation creep regimes (Hirth & Tullis, 1992) were examined. Regime 1 is characterized by a high yield strength and substantial strain softening and non-recrystallized grains deforming by fracturing and dislocation glide (Hirth & Tullis, 1992) and climb (Stipp & Kunze, 2008) while recrystallization occurs by bulging or nucleation and growth of new grains. Aggregates of newly formed grains are thought to deform by a dislocation process with a substantial contribution of grains boundary sliding (Tullis, 2002; Stipp & Kunze, 2008). Regime 2 samples yield at lower stresses and no pronounced weakening is observed. Incipient subgrain rotation recrystallization (SGR) has been documented (DellAngelo & Tullis, 1989). Regime 3 exhibits the lowest flow stresses, SGR is predominant, and some workers observe synkinematic normal grain growth (Gleason et al., 1993; Stipp et al, 2006) or abnormal grain growth (Heilbronner & Tullis, 2006), potentially in relation to texture development.

Solid Earth Discuss., doi:10.5194/se-2017-44, 2017
Manuscript under review for journal Solid Earth
Discussion started: 19 May 2017

Specific types of textures and certain texture components have been given genetic or descriptive terms in the literature. In particular,grains with a specific c-axis direction have been interpreted to be suitably oriented for the activity of specific slip systems with the <a>-direction as a Burgers vector and have therefore been called ‘basal-’, ‘prism’ or ‘rhomb-grains’ (Bouchez & Pecher, 1981; Heilbronner & Tullis, 2006). Here we will call grains with the c-axis at the periphery of the pole figure, and approximately orthogonal to the shear plane B-grains or B-domains, those contributing to the intermediate parts of a single girdle, between the periphery and the centre will be termed R-grains or R-domains, those with peripheral c-axes inclined against the sense of shear, roughly towards the direction of the loading piston will be termed σ-grains or σ-domains and finally those grains with c-axes close to the centre of the pole figure Y-grains or Y-domains on account of their proximity to the Y-direction in the inferred strain reference frame.

2. Methods

2.1 Experiments & samples:

The analysed samples are experimentally deformed Black Hills Quartzite (BHQ) of Heilbronner & Tullis (2002 and 2006). 1 to 1.5 mm thick slabs of BHQ were deformed in a solid medium, modified Griggs-type deformation apparatus. The slabs were placed between two 45° pre-cut forcing blocks made up of single crystal Brazil quartz oriented with the c-axis parallel to the advancing load piston. Experiments were performed on “as-is” BHQ and with 0.17 wt. % H_2O added (~11000 ppm H/10^6Si) in mechanically sealed PT jackets. “As-is” experiments were conducted at 850 °C and water added experiments at 875 and 915°C, all an axial shortening rate of ~3*10^-5 s^-1 and confining pressures of 1.5 GPa. Details of the experimental procedures are provided in Heilbronner & Tullis (2002, 2006) and in the companion paper Heilbronner& Kilian (this volume). Sample strain or flow related reference directions such as the principal

Solid Earth Discuss., doi:10.5194/se-2017-44, 2017
Manuscript under review for journal Solid Earth
Discussion started: 19 May 2017

Solid Earth
Discussions
Open Access
EGU

strain axes or the instantaneous stretching axes(ISA) were calculated from final displacement, initial and final sample thickness assuming steady general shear (e.g. Fossen & Tikoff, 1993).

2.2 EBSD data analysis

EBSD maps were collected on a Zeiss Merlin FEG-SEM, equipped with am Oxford (insert. details here) EBSD Camera in low vacuum mode, using a 2x2/4x4 binning, 20 kV acceleration voltage, and a probe current of 6-9 nA using step sizes of 0.5 and 1 µm and exceptionally 0.25 µm. Unless otherwise specified, only the maps of the high bulk strain experiments w1092, w946 and w1092 were analyzed (details are given in Heilbronner & Kilian, this volume). Data cleanup and all processing was done using the mtex toolbox by Ralf Hielscher (Bachmann et al. 2011; Mainprice et al., 2014; https://mtex-toolbox.github.io/). See appendix for details on data processing.

Textures are presented in the form of (inverse) pole figures using the point group '321' for quartz (Fig. 1). Pole figures are displayed such that normal to the shear zone boundary (surface of the forcing blocks of the experiment) is vertical and the displacement direction horizontal. Texture strength is given as texture index, pole figure J-index and maxima of pole figure densities. See appendix for details on texture calculations. Crystal directions or poles to planes of (0001),[0001],< 11-20>, {10-10}, {10-11} and {01-11} are abbreviated as (c), [c], <a>, {m}, {r}, and {z} with the conventional bracketing scheme.

Positions on the pole figure will be given as azimuthal angles with an origin in the west, increasing clockwise, inclination being 0 in the centre of the pole figure. Directions in the first and third quadrant (NW and SE) are inclined with a sinistral sense of shear.

Textures have been calculated for classes of grains in aspect ratio - grain size, and long-axis trend (θ) - aspect ratio space. Grains from different maps of identical step size of low and high total strain experiments of each regime have

Solid Earth Discuss., doi:10.5194/se-2017-44, 2017
Manuscript under review for journal Solid Earth
Discussion started: 19 May 2017

been combined to obtain a sufficiently large datasets. Class boundaries are chosen such that they are equally populated for each property and combinations of two properties result in a 3-by-4 matrix in e.g. aspect ratio – grain size space. Because distributions are skewed, classes are note equally populated. Kernel parameters for the texture calculations were estimated individually for each class and since that, pole figure geometries are comparable and densities of pole figures will not be overestimated for poorly populated classes.

Spherical interpolations for grain size, aspect ratio and axial ratio have been calculated in c-axis pole figure space. They represent the average grain property at a given c-axis direction. To avoid a bias introduced by the uneven distribution of c-axis poles the following procedure was used: A subsample of 400 grains was drawn, the c-axis direction was calculated, the property associated with each grain was interpolated on a 15° spherical grid using an inverse distance weighting, the procedure was repeated 1000 times and the mean of the interpolation was plotted as a pole figure.

Grain sizes are defined as the diameter of an area equivalent circle of the grains. The grain long axis and aspect ratio are obtained from the best fit ellipse from smoothed grain boundaries.

To quantitatively compare texture strength of the grain property classes (e.g. grains size – aspect ratio classes), subsamples of identical sizes were estimated in a bootstrapping approach. 100 randomly chosen subsamples of the size of the smallest of any population (>100) were repeatedly drawn from the population of grains within a property class. Texture parameters were calculated for each subsample using a fixed kernel width. The mode of the resulting distributions is compared. The standard deviation usually converged after <50 draws to below 5-10%. Texture strength was measured using the texture index (texture or J-index, L2-norm of the ODF) and two different fibre volumes. A fibre is defined by a crystal direction and a corresponding direction in specimen coordinates and manifests as a line in ODF space. The fibre volume is the mass fraction of an ODF contained within a radius around a given fibre. One fibre (B-fibre) is defined by the

Solid Earth Discuss., doi:10.5194/se-2017-44, 2017
Manuscript under review for journal Solid Earth
Discussion started: 19 May 2017

Solid Earth Discussions

[0001] direction inclined 76° to the shear plane with the sense of shear (B-fibre) and another fibre (Y-fibre) is defined by the [0001] direction pointing towards the centre of the pole figure (structural y-direction). For easier inspection and comparison, results are colour-coded and plotted in x-y parameter space (aspect ratio - grain size or θ - aspect ratio).

Misorientation axes have been determined in specimen and crystal coordinates for misorientation angles of 2-9° for subsets of grains. Subsets a chosen to contains grains with modal orientations of up to 25° away from the orientation modes for Y-, B-, R-, and sigma-grains. This threshold angle corresponds to a volume in the ODF and not to the opening angle of a cone on a [c] pole figure, making the selection stricter compared to Heilbronner & Tullis (2006) since thresholds are applied to modes of orientations and not only c-axis directions. Pole figures and inverse pole figures are contoured as well as a random subsample of points is plotted. Individual points are colour-coded such that misorientation axes in specimen reference frame appear in the colour key of the axis in the corresponding crystal reference frame. Misorientation axes in crystal reference frame are colorised by the inclination of the axis in specimen coordinates.

<a>-intransparency is defined as the minimal angle between <a> across a grain boundary, ignoring the polarity of <a> and it is a measure of strain compatibility of adjacent grains deforming by glide along <a> on an infinite group of planes.

The grain kernel average misorientation (gKAM) is calculated from the kernel average misorientation (KAM) from noise reduced EBSD data. The gKAM is the sum of the KAM within a grain divided by the number of measurements with the grain. The gKAM is a measure of intragranular deformation intensity or misorientation density and depends on the misorientation angle and fraction of low angle boundaries within a grain. See appendix for details.

Solid Earth Discuss., doi:10.5194/se-2017-44, 2017
Manuscript under review for journal Solid Earth
Discussion started: 19 May 2017

The generalized Schmid factor Sf (Reid, 1973) is calculated from a given slip system and a stress tensor, and presents the ratio between the shear stress on a slip system and the norm of the macroscopic stress tensor. Since the general shear experiments are plane strain and displacement is resolved parallel to the dip of the forcing block, we use a triaxial, normalized stress tensor. The absolute magnitude of the stress tensor does not have any influence on the value of the generalized Schmid factor. Schmid factors are calculated for all orientations (either each measurement or grain modal orientation), and their sum is divided by the number of orientations. For combinations of slip systems, Schmid factors are calculated for all slip systems in the combination and the maximum values are averaged.

3. Results

3.1 Pole figure geometry

In the regime 1, the pole figures show a broad, asymmetric peripheral distribution of c-axes with a maximum ~78° (inclined with the sense of shear) (Fig.1a). Minor densities occur at ~130° roughly parallel to the shortening axis in the experiment and a tail towards the centre of the pole figure. <a> shows a major maximum at the periphery, forming an angle of ~-12° with the shear plane. Two minor maxima of <a> lie on great circles inclined about 15° with respect to to the pole figure centre. Poles to {r} shows a symmetric peripheral maximum inclined against the sense of shear at ~+120° and a girdle distribution perpendicular to the peripheral maximum.

In the regime 3 sample, c-axes pole figures show an elongated maximum in the centre of the pole figure, overlying a weak, kinked single girdle. Internally the maximum is composed of two maxima at an angular distance of about 20°, symmetrically arranged above and below the shear plane. A-axes form a major maximum at ~-10°.

Solid Earth Discuss., doi:10.5194/se-2017-44, 2017
Manuscript under review for journal Solid Earth
Discussion started: 19 May 2017

Solid Earth Discussions

In pole figures obtained from regime 2 experiments, [c] is distributed along a kinked single girdle, presenting a combination of regime 1 and 3 pole figures. A-axes form a strong maximum at ~-13° and the {r} pole figure resembles the one observed in the regime 1 sample.

Minor but significant densities of [c] in the pole figure are positions inclined against the sense of shear (roughly corresponding σ-directions) are only found in the regime 1 samples.

Inverse pole figure (IPF) have been constructed for various strain and sample related reference directions (Fig. 1b): in general and most dominant in regime 1 and 2, the strongest alignment is found for <a> and a reference direction of the ISA1 - 45°, (-10° below the shear plane, being the trace of the highest shear stress). In the regime 3 sample, <a> also shows a strong alinement with the shear direction since it is generally more strongly dispersed around the periphery. In IPFs with a reference direction at 135° (parallel to the direction of the load piston), all samples show a high density very close to {20-21}. Using the shortening ISA (being steeper than the direction related to the load piston) as a reference direction, in regime 1 and 2 a very strong alignment of {r} is found.

3.2. Orientation maps.

Based on the result of the IPFs, we display orientation maps in an inverse pole figure colour coding with respect to the ISA1-45° (Fig. 2a). Maps show a relatively homogeneous distribution of <a> parallel to the reference direction across all three samples. Notably in regime 1 and 2 samples, inside bands with a shear band geometry,dispersed grains show an alignment of [c] close to the shear plane.

Solid Earth Discuss., doi:10.5194/se-2017-44, 2017
Manuscript under review for journal Solid Earth
Discussion started: 19 May 2017

Using the structural Y-direction as a reference (Fig2b), the increase from regime 1 to 3 in orientations with [c] parallel Y can be clearly seen. In regime 2 it appears that tY-grains dominate in areas mostly devoid of larger porphyroclasts and a smaller grain size. In regime 3 Y-grains also occur in a spatially domainal structure.

3.3 Variation of pole figure geometry within classes of grain size, aspect ratio and long axis direction

For pole figures calculated in aspect-ratio-grain size space, the following observations are made (Fig.3): For all regimes, [c] pole figures show and increased ordering towards higher aspect ratio and towards larger grain sizes. In regime 1 small grains in general show the broadest distribution, dispersed along the periphery. With increasing aspect ratio, a weak single girdle can be recognised. In regime 3, [c] pole figures obtained from large grains with the large aspect ratios show the highest degree of ordering with the elongated central maximum and peripheral maxima and minor off-periphery maxima, forming a single, kinked girdle. In pole figures calculated for regime 2 experiments, the identical relationship is observed, a single kinked girdle develops with peripheral and central maxima, which can be described as mixtures between regime1 and regime 2 pole figures (Fig.3).

For pole figures of θ – aspect ratio classes, in general those [c] pole figures from within classes of the largest aspect ratio and θ containing the maximum of the trend distribution have the highest degree of ordering. Second strongest [c] alignments are found for regime 1 in the θ class which contains the trend of the shear plane and for regime 2 and 3 the θ class with steeper major axis trends. The weakest [c] ordering can be found in those classes containing grains with a θ pointing against the sense of shear. While the distribution of maxima along the girdle characteristically varies from regime 1 over regime 2 to 3, additionally

Solid Earth Discuss., doi:10.5194/se-2017-44, 2017
Manuscript under review for journal Solid Earth
Discussion started: 19 May 2017

within each regime, the classes with the highest aspect ratios and within those, the θ class for most well aligned grains, show an increasing concentration of [c] in central regions of the girdle.

The position of the peripheral part of the kinked girdles shows a consistent variation with the θ class, being most inclined (with the sense of shear) in those classes also containing the trend of the shear plane and being steepest within the classes of θ steeper than the maximum (table 1). This variation is most expressed for classes of high aspect ratio.

To summarize, the pole figure skeleton, the density along the girdle and its inclination varies with θ and the deviation of [c] maxima on the girdle from the periphery depends most on grain aspect ratio.

Pole figures for <a> and {r} for the different classes of grain size, aspect ratio and θ are far less subject to changes in geometry and exemplified for regime 2 samples (Fig. 4). <a> readily form peripheral maxima close to the shear plane and ordering increases with increasing grain size and aspect ratio. Pole figures for {r} show the peripheral maximum at ~110-120° which varies together with the trend of the [c] girdle (Table 1).

In a few cases, a secondary, peripheral [c] maximum (or relict cross girdle) is present and its opening angle varies between 50° to about 80°, mostly as a function of aspect ratio but not systematically between regimes.

3.4 Pole figures of grain properties

For pole figures of grain size, aspect ratio and axial ratio (Fig. 5) obtained from a subset of grains smaller 25 µm, for regime 1 and 2 the average grain size (comparable to a number weighted average grains size) is largest at the periphery and for regime 3, it is largest in the centre of the [c] space. In all three regimes,

Solid Earth Discuss., doi:10.5194/se-2017-44, 2017
Manuscript under review for journal Solid Earth
Discussion started: 19 May 2017

a high average aspect ratio is found along a kinked girdle for regime 1 and 2 and a weak cross girdle for regime 3. The largest average aspect ratios along these girdles are located at the centre of the girdle for regime 2 and 3. Inversely, the largest average axial ratio occurs for grains with [c] in one of two close to orthogonal, peripheral directions, roughly at 30-35° or 125°.

3.5 Pole figures for low-gam/high gam grains

Pole figures are calculated for populations of grains with a gKam below and above the median gKam, independent on grain shape or size parameters. The most obvious difference between the textures for low and high gKam classes are seen in the c-axis pole figures for recrystallized grains (Fig. 6a). Here, grains < 12 µm for regime 1 and 2 and < 25 µm for regime 3 are considered. In general [c] pole figures for the high gKam population show a stronger degree of ordering and a tendency for higher pole densities away from the periphery, along the kinked single girdle. The higher degree of ordering is expressed by an creasing the pfJ, higher densities along the girdle, narrower peripheral maxima and in the case of of single maximum pole figures also by the magnitude of the maximum. Peripheral maxima shift to Y-maxima (regime 2) or secondary peripheral maxima disappear in the high gKam classes. This trend is more pronounced in textures calculated from all the orientations from within grains within a given class. For <a> and {r} pole figures, mostly a strengthening of the maxima at the periphery can be noticed. Comparing pole figures obtained from the uppermost and lowermost 20% of the gKam population, this change in geometry is even more pronounced (Fig.6b).

3.6 Quantification of texture strength

In all regimes, the texture index increases with increasing aspect ratio and for higher aspect ratios also for increasing grain size (Fig. 7). Also, the classes containing the (recrystallized) grains with the largest size and aspect ratio possess the highest texture strength. In each regime and class, there is also an increase in the texture index from those population of grains with a low gKAM to those

Solid Earth Discuss., doi:10.5194/se-2017-44, 2017
Manuscript under review for journal Solid Earth
Discussion started: 19 May 2017

Solid Earth Discussions
Open Access

with a high gKAM (0.05-0.55 and >0.55°). For regime 2, there is an additional maximum for small grains with high aspects ratios within the higher gKam class. Within θ - aspect ratio space, it is observed that the texture index continuously increases towards higher aspect ratio. In regime 1 the highest texture index is found for high gKAM classes at θ of ~20-30°. In regime 2 the range of the texture index is smaller but still maximum values are found for high aspect ratio classes with a θ containing the shear plane or in the class of 20 to 40°. For regime 3, also high aspect ratio classes have the highest texture index with the maxima found clearly off the shear plane in the 30-45° θ bin. For all regimes, there is an increase in the maximum texture index form the low gKAM to the high gKAM class.

For aspect ratio - grain size classes and θ - aspect ratio classes the volume of the B-fibre is largest for regime 1 and smallest in regime 3 while in contrast, the volume of the Y-fibre is smallest in the regime 1 samples and largest in regime 2 samples, reflecting what can be roughly seen in the pole figures. The variation of B-fibre volumes within regime 1 and y-fibre volumes within regime 3 is comparable to trend in variation of the texture index in the corresponding classes; also with an increase in fibre volumes form low gKAM to high gKAM classes in θ - aspect ratio space for regime 1 and regime 3 as well as in aspect-ratio - grain size space in regime 3. Regime 2 does not show a large variation in B- and Y-fibre volumes (since c-axis girdles host both components), however, there is a small decrease in volumes of B-fibres and in increase in the volumes Y-fibres from low gKAM to high gKAM classes.

3.7 Structure of Y-domains and misorientation axes related to low angle boundaries

Figure 8a shows a crop of an EBSD map of a Y-domain with a colour coding of boundaries based on the <a>-intransparency. While c-axes are strongly aligned, the <a>-intransparency can have relatively high angles (>20°) and may change

Solid Earth Discuss., doi:10.5194/se-2017-44, 2017
Manuscript under review for journal Solid Earth
Discussion started: 19 May 2017

Solid Earth Discussions

gradually along grain boundaries. Low values of the <a>-intransparency between grains with c-axes at a high angle to another are also present, however, less frequent than low values of the <a>-intransparency between y-grains. Grain boundaries of the Y-grains show in total a larger deviation from the uniform distribution of the <a>-intransparency with more lower and more higher angles for boundaries between Y-grains (see Appendix A2), while inter the latter approaching a distribution which would be expected for a uniform texture.

colour-coding low angle boundaries for their misorientation axis in crystal coordinates shows that most low angle boundaries within a y-domain have a rotation axis close to the c-axis (Fig. 8b). However, other directions are also present and in non-Y grains, rotation axes close to one of the poles to rhombs or of directions located within the basal plane appear to be more frequent.

Misorientation axes are shown for a regime 2 sample for Y-, B-, and R-grains (Fig. 9). For the complete dataset for all three regimes including sigma grains see Appendix 4. Misorientation axes dominate around the c-axis direction, also coinciding with the axes being most inclined (parallel to the kinematic y-direction). For B-grains, the highest density of misorientation axes is found to have directions within the basal plane, mostly close to m. However, the strength of this distribution is very weak. R-grains show a maximum of misorientation axes around c and a slightly higher density in the area of positive rhombs. Misorientation axes with direction most closely parallel to the kinematic Y-direction preferentially fall close to a position between the <10-11> and a more general direction ~ <7-2-56>. For σ-grains, a distribution is found similar to that of the b-grains, however with a slightly more pronounced deviation from uniformity (see Appendix 4). For all grain classes it can be seen that a variably strong maximum of misorientation axes in specimen coordinates is parallel to the kinematic Y-direction. R-grains show the highest density of misorientation axes in crystal coordinates around the c-direction while in specimen coordinates, the maximum is located also at the kinematic Y-direction. Since this is in the first place a contra-

Solid Earth Discuss., doi:10.5194/se-2017-44, 2017
Manuscript under review for journal Solid Earth
Discussion started: 19 May 2017

Solid Earth Discussions

dictory situation, is needs to be noticed that the distribution of misorientation axes in specimen coordinates is elongated towards axes which correspond to rotations around the c-axis (red clusters, third column in Fig. 9d), while those misorientation axes located at the centre of the pole figure correspond those crystal directions loosely located between 10-12, 10-11 and <7-2-56>.

3.8 Schmid factor analysis

The mean generalized Schmid factor is plotted as function of the trend of the maximum principal stress direction of the stress tensor (Fig. 10). Highest Schmid factors are attained for $\sigma1$ directions consistently about 10 to 20° steeper compared to the direction of the load piston. For single slip systems, in all regimes, disrespect of whether modal grain orientations or all points of the EBSD maps are used, {pi'}-<a> or {z}-<a> give the highest Schmid factors. Notably also in regime 1 where many grains have [c] at the periphery of the pole figure, highest mean Schmid factors are predicted for {pi'}-<a>. For combinations of slip systems, in regime 2 and 3, {m}-<a> + {pi'}-<a> + {z}-<a> always give the highest mean Schmid factors and are equally high in regime 1 as the combination of {m}-<a> and (c)-<a>. Notably, the curve for {m}-<a> shows a similar behaviour as the curve for <a> slip on the positive rhombs, having a minimum mean Schmid factor at the position where for most reasonable slip systems show a maximum. While this is logical for {r} and {z} for example, {m} have this crystallographic dependency and this behaviour is somewhat unexpected.

Solid Earth Discuss., doi:10.5194/se-2017-44, 2017
Manuscript under review for journal Solid Earth
Discussion started: 19 May 2017

4. Discussion

Textures of recrystallized grains and bulk textures of all regimes share an alignment of <a> to the direction of parallel to the trend of the plane of maximum shear stress at ~-10° within the shear plane and a strong alignment of the positive rhombohedral planes towards the shortening ISA (regime 1,2). There is a transition in texture geometry (skeleton) and in texture strength across the regimes. [c] is dispersed on the periphery normal at a high angle to the shear plane in regime 1, distributed along a kinked, single girdle in regimes 2 an forms a central bi-modal maximum at the structural Y-direction in regime 3. The texture strength increases from regime 1 to regime 3.

Similar pole figure skeletons have been reported in nature (e.g. Bouchez & Pecher, 1981; Mancktelow, 1987; Law et al., 1990) and similar texture transition were observed within metamorphic gradients (Stipp et al., 2002). Occasionally this type of transition was used to draw inferences on the metamorphic conditions for mylonitisation (see Law, 2014 for a review). In experiments, a texture transitions was observed in axial compression experiments (Tullis et al., 1973), where in the high stress regime [c] pole figures have a single maximum parallel to the compression axis and in low stress regime, [c] occurs within a small circles centred around the compression axis. Some types of texture transitions observed in nature (e.g. Lister & Dornsiepen, 1982; Gapais & Barbarin, 1986) were often explained to be related to the activity of prism-c slip at very high temperature (e.g. Mainprice et al., 1986). Based on the speculation on a temperature dependency of different <a>-slip systems (Blacic, 1975; Hobbs, 1985), certain types of textures were thought to be related to <a>-slip on different planes. However, those texture transitions with evolving densities along a single or cross girdle (e.g. Stipp et al., 2002, Toy et al., 2008) are difficult to explain with a hypothesis of temperature sensitive <a>- slip systems and factors such as strain, alternative texture forming processes and the influence of recrystallization mechanisms are variables that need to be taken into account as well.

Solid Earth Discuss., doi:10.5194/se-2017-44, 2017
Manuscript under review for journal Solid Earth
Discussion started: 19 May 2017

In the analysed experiments, the temperature difference was only about 65° and displacement rates and finite strains are roughly identical in all regimes and the major difference observed for these samples is the peak and flow stress (Fig. 2). Accordingly, a temperature and bulk strain rate dependence can be neglected, and the effects of the recrystallization and texture forming mechanisms of samples deforming at basically identical conditions but different flow stresses can be studied.

4.1 Relation of the texture transition to deformation intensity at the grain scale

Increasing central densities along a (partial) girdle are documented especially for regime 2 and 3 with increasing grain scale deformation. We will take the θ – aspect ratio relation and the gKAM as a measure for grain scale deformation. Based on the coincidence of the maximum in the distribution of θ with the ISA and the observation of the most synthetically rotated girdles in the θ classes which contains the direction of the long axis of the finite strain ellipsoid (Fig 3), grain alignment is assumed to be related to deformation. Similarly, we assume that grain lengthening is related to deformation. If strain at the grain scale is achieved via a dislocation mechanism, and if low angle boundaries are the result of dynamic recovery by a climb of the strain producing slip system, the gKAM is an expression of the intragranular deformation intensity. These assumptions are supported by the observation of an increased texture strength with increasing grain lengthening, alignment and increasing gKAM. We will argue that the regime 3 sample shows the strongest support for dislocation creep and that dynamic recrystallization is dominated by subgrain rotation, and therefore a high texture strength is associated with dislocation creep and this includes glide which is the texture forming process.

With respect to the [c] pole figure skeleton an increasing ordering, development or strengthening of a girdle component and/or the formation of a central maximum can be related to grain scale deformation. All these observations (Fig. 3,6) indicate that [c] moves away from the periphery of the pole figure as grains deform. Given that the BHQ starting material shows a close to uniform texture, the the Y-maximum is strain induced with [c] rotating along the single girdle towards the centre of the pole figure. In nature, very similar textures evolutions are reported as a function of bulk shear strain (Pennacchioni et al., 2010) and also there, even at the highest observed shear strains, [c] only approaches the Y-direction. It remains to be explored whether this rotation is continuous or if there are temporarily stable orientations. Positions of slow rotation rate might yield the occasionally reported "rhomb"-maxima, although the exact c-axis positions are quite variable and may be depend on other factors such as the kinematics of flow as well.

In contrast, in regime 1 we observe a large volume of grains with [c] at the periphery of the pole figure which must originated from the uniformly textured BHQ and their occurrence cannot be explained by the observed strain related evolution of orientations.

4.2 Textures as indicators of deformation mechanism

4.2.1 Deformation mechanisms

Quantitative analysis of texture strength may give direct information on the contribution of texture forming processes. Because an estimation of texture strength depends on many variables, estimators should always be conservative in the sense of not overestimating texture strength and because in geologic materials, there is no knowledge about the exact meaning of absolute values, we performed a quantitative comparison. Absolute densities and hence texture strength is expected to underrepresent the density of the underlying "true" distribution but relative differences are quantitatively comparable in the presented approach (Fig. 7).

An increase in texture strength from regime 1 to regime 3 is documented as well as a strengthening of the texture with increasing grain scale scale deformation. The strength of a texture originating from deformation is usually related to the contribution of crystal plastic mechanism such as dislocation glide and climb. At the other hand, it can also be shown that crystal orientations and grain shapes show a specific relationship since e.g. [c] girdles rotate as a function of θ (Fig. 3, Table 1), which suggests that a certain amount of grain rotation takes place in the forma of rigid body rotation and not entirely related to the internal deformation of the grains. Such a relative grain movement requires grain boundary sliding. The necessity of grain boundary sliding during dislocation creep is well known in some metals (e.g. Kottada & Chokshi, 2007) and has been suggested for quartz mylonites (e.g. Mancktelow, 1987; Kilian 2011a) as a process related to strain compatibility (Zhang et al., 1996). Glide with the involvement of a prism-a slip system induces grain rotation around [c] within a Y-domain which will result in strain incompatibility with the neighbouring grain as seen in the occurrence of large angles for the <a>-intransparency (Fig. 8a) which fits the suggestion in the literature (Mancktelow, 1987) that this type of behaviour would be expected for a texture with a Y-maximum.

In regime 1small grains have [c] broadly dispersed along the periphery (Fig. 6,7) and with increasing aspect ratio and grains size of recrystallized grains, [c] gathers towards the peripheral edge of a partial single girdle and the texture strength is much lower compared to the regime 3 sample it is likely that the contribution of grain boundary sliding in regime 1 is larger. Grain boundary sliding has been suggested to significantly contribute to deformation in regime 1(Tullis, 2002; Stipp & Kunze, 2008). Possibly, in regime 1, the newly formed grains are rather undeformed and may be smaller than the equilibrium subgrain size, leading to grain boundary sliding which correlates with the observation of the very broad dispersion of [c] at the periphery for low gKAM grains in regime 1 (Fig. 6b).

In summary, the contribution of dislocation creep is interpreted to be largest in regime 3 and the contributions of grain boundary sliding is largest in regime 1 and smallest in regime 3 samples. Since all mechanisms operate concurrently, observed changes in texture strength are a result of different contribution of

Solid Earth Discuss., doi:10.5194/se-2017-44, 2017
Manuscript under review for journal Solid Earth
Discussion started: 19 May 2017

each individual process. Regime 2 is again envisaged to n an intermediate situation – more dislocation creep contribution than in regime 1 and more grains boundary sliding contribution than in regime 3.

4.2.2 Recrystallization processes

Porphyroclasts usually show systematic substructures characterized by discrete orientation domains of a size comparable to the recrystallized grains size. In regime 2 and especially regime 3, orientation domains are recognized which are roughly of the size of original BHQ grains (Heilbronner & Kilian, this volume) but are fully recrystallized. The progressive change in grain orientation with respect to their neighbours in Y-domains in regime 3 is compatible with rotation of parts of the crystal around misorientation axes parallel to the vorticity axis inferred for the experiment (Fig. 8 a,b). All these microstructures are compatible with SGR recrystallization. In regime 1 where bulging recrystallization is dominant (Hirth & Tullis, 1992, Stipp & Kunze, 2008) a large fraction of recrystallized grains attain a new orientation, unrelated to a host derived orientation domain. Besides, that the lack of an orientation relation with the host may also result from a contribution of grain boundary sliding, smallest, most equiaxed grains have the highest c-axis densities at a peripheral position (Fig. 5) and poles to {r} align towards the shortening direction. The exact nature of the process that controls the orientations of newly formed grains during bulging recrystallization remains unclear and there are controversial suggestions in the literature (e.g. Stipp & Kunze 2008; Cahn & Mishin, 2009). For all larger grains, it is reasonable to assume that the clustering of poles to {r} to {pi} (the latter closest to the elastically softest direction) at the shortening direction is the result of Dauphiné twinning (e.g. Tullis & Tullis, 1972) caused by a rotation of {z} away from the shortening direction around the c-axis. Because Dauphiné twinning does not affect the direction [c] and a fibre-texture around {pi} or {r} is not strongly developed, a

Solid Earth Discuss., doi:10.5194/se-2017-44, 2017
Manuscript under review for journal Solid Earth
Discussion started: 19 May 2017

different process needs to be responsible for the preferred occurrence of [c] at the periphery in regime 1. Preferred growth is one such process and the potential will be discussed within section 2.4.

4.2.3 Evidence of active slip systems

Although, the interpretation of slip systems based on misorientation carries uncertainties because the direction of subgrain boundaries is not known from 2D sections, it supplies more information compared to a purely pole figure or deformation lamellae based speculation. Most misorientations in y-domains (Fig 9., Appendix 4) are compatible with a dominance of a {m}<a> slip system and because axes in specimen coordinates coincide with the inferred vorticity axis, there is a high probability of a tilt character for boundaries trending parallel to {a}.

The R-domains show a distribution of axes in specimen coordinates which appears elongated towards the positions of the [c] in the pole figure. The superposition of the two populations of misorientation axes roughly parallel to c-axes results in a maximum density around [c] in crystal coordinates. This situation points to the necessity to interpret density contoured misorientations axis plots carefully, because the representation in crystal coordinates honours crystal symmetry which may result in high densities of superposed misorientation axes which are physically different in specimen coordinates. Linking misorientation axes in both coordinate systems via a common colour coding such as the one used here can an example (Fig. 9) to overcome this problem. Misorientation axes in the R-domain which appear parallel to the vorticity axis reside in the position close to <10-11>, <10-12> and ~<7-2-56>. The first and second direction are compatible with {pi'}-<a> and {z}-<a> glide, respectively; both slip systems have been identified in nature (e.g. Morales et al., 2011), experiment (e.g. Linker et. al. 1984) or suggested based on texture and Schmid factor considerations (Law et al., 1990). Proximity to <7-2-56> could theoretically, in the case of a tilt character, correspond to {s}-<c-a>which might be doubted to operate since the fairly

Solid Earth Discuss., doi:10.5194/se-2017-44, 2017
Manuscript under review for journal Solid Earth
Discussion started: 19 May 2017

high length of the burgers vector. In general, misorientation axes of the R-domain are compatible with the oblique activation of {m}-<a> as well as any of the {z}- or {pi’}-<a> slip systems. This interpretation is compatible with the persistence of <a> aligned with the trend of the plane of highest shear stress while [c] rotates towards the centre of the pole figure along the kinked girdle.

The misorientation axes of the B-domain show a distribution close to uniform. In the case of (c)-<a> activity and the presence of tilt boundaries, misorientation axes are expected to be clustered around <m> and in the case of conjugate slip, to disperse in specimen coordinates along the trace of the basal plane. In the case of twist boundaries, the rotation axes would be expected normal to (c), which will be in the situation of the B-domains at a high angle to the shear plane. Since neither of this is strongly pronounced, it might be that (c)-<a> is not one of the slip systems being most active in the B-domain.

The above interpretation seems to be compliant with the Schmid factor analysis (Fig. 10), where overall high Schmid factors are found for {pi'}-<a>, {z}-<a> and partially {m}-<a> with an orientation of the maximum principal stress axes aligned with the shortening ISA.

4.2.4 A model for the texture development and texture transition

As outlined above, a deformation-dependent rotation of [c] away from the periphery of the pole figure is observed, it is found that most likely {m},{z} and {pi’}<a> slip systems operate together and that evidences of (c)<a> are scarce but there is no indication that any of the above described processes and mechanisms contributes to the presence of grains with [c] at the periphery of the pole figure as mostly encountered in the regime 1 sample.

The principal difference in that suite of experiments is the sample strength. Because displacement rate constant and temperature differences are vey small in the current experiments, it is controlled through the amount of water added to experimentally deformed quartzites (e.g. Kronenberg & Tullis, 1984; Jaoul et al.,

Solid Earth Discuss., doi:10.5194/se-2017-44, 2017
Manuscript under review for journal Solid Earth
Discussion started: 19 May 2017

Solid Earth
Discussions

1984). Despite early speculations that different water contents having an influence on the activity of specific slip systems (e.g. on synthetic single crystals, Blacic, 1975), the role of water is mainly related to control the mobility of grain boundaries in polycrystalline quartz aggregates (e.g. Gleason et al., 1993; Stipp et al. 2006) as well well as in naturally deformed rocks (e.g. Mancktelow & Pennacchioni, 2004; Kilian et al, 2016). The amount of water present in the the "as-is" samples is still sufficiently high to hydrolyse dislocations even at high densities (e.g. Paterson, 1989) and the overall weakening effect will rather be a result of the enhanced recovery processes. Accordingly, a direct relation of water to the texture transition through a crystal plastic mechanism can be most likely excluded.

We suggest a model in which the texture transition can be explained based on the hypotheses that a) during SGR and dislocation glide, [c] moves towards the centre of the pole figure along seemingly well defined paths which constitute the girdle and that b) an additional process operates that produces new grains (new grain formation NGF) with [c] at the periphery of the pole figure at a high angle to the shear plane which operates at higher stress levels. Both texture forming processes compete, with the first one being dominant in regime 3 and the second one being dominant at high stresses in regime 1. Regime 2 is a transition where both contributions might be roughly balanced.

In regime 3, most SGR occurs and recrystallization is fastest, hence the rotation of [c] towards the Y-direction will be happening most rapidly, NGF does not happen substantially, hence not many new grains are formed with [c] at the periphery. All large grains are recrystallized in the high strain experiments. In regime 1, NGF occurs most and SGR is slowest, the matrix of small grains deforms with a fair distribution of grain boundary sliding, hence the rotation of [c] towards the centre is slow and [c] is dispersed along the periphery. Because strain partitions into the matrix, porphyroclasts that stretch most effectively are those that survive longest.

Solid Earth Discuss., doi:10.5194/se-2017-44, 2017
Manuscript under review for journal Solid Earth
Discussion started: 19 May 2017

Several lines of evidence support a mechanism such as NGF. There is ample indication that growth of new grains after fracturation, or in most highly strained crystals and in general under non-hydrostatic stresses during deformation can result in a moderate to strong crystal preferred orientation in experiments (e.g. Hobbs, 1968; Gleason et al., 1993; Vernooij et al, 2006; Trepmann et al., 2007; Trepmann & Stöckert 2013) and in nature (e.g. Hippert, 1994; Hippert & Egydio-Silva,1996; Menegon et al. 2008; Spiess et al., 2012; Kjöll et al. 2015). Newly formed grains are found to have [c] roughly parallel and less commonly orthogonal to the (inferred) shortening direction (e.g. Hobbs, 1968; Gleason et al, 1993; Trepmann & Stöckert, 2013; Kjöll et al. 2015), or roughly at 45° to the stretching direction of shear fractures (e.g. Vernooij et al., 2006; Trepmann et la. 2007; Menegon et al., 2008). Fracture and microfracture development have documented in the Griggs-rig, even at high confining pressures and is thought to be an essential process to enable crystal plasticity in the experiments (FitzGerald et al., 1991; denBrok & Spiers, 1991; Stünitz et al., 2017). This might most likely applies also to BHQ during initial steps of deformation and large porphyroclasts, as well as quartzites deforming in the hardening regime with limited grain boundary mobility (Hirth & Tullis, 1992). The positions of grains with high axial ratios provides [c] directions (Fig. 5) which can be compatible with newly formed grains, which have orientations subsequently modified by grain boundary sliding and crystal plastic processes while they grow. The occurrence of shear band -like features with c-axes roughly aligned with the opening/stretching direction of the bands (Fig. 2) can be taken as indication that also a local kinematic framework oriented grain grow with a preferred orientation. We do not have any direct evidence of a fracture/nucleation/growth origin of grains newly forming in the regime 1, however, in most experimental studies B-domains seem to be the first to form at high stress conditions and e.g. the texture transition observed by Tullis et al. (1973) perfectly matches our model with preferred growth of [c] parallel and to a very minor amount perpendicular to the shortening direction. Whether the resulting texture in regime 1 relates to anisotropic growth controlled purely

Solid Earth Discuss., doi:10.5194/se-2017-44, 2017
Manuscript under review for journal Solid Earth
Discussion started: 19 May 2017

by nucleation and growth under non-hydrostatic stresses, influenced by the elastic anisotropy of quartz or is additionally influenced by the local kinematics of quartz must remain to be evaluated in future studies.

4.3 Peripheral c-axes are not due to (c)<a> slip?

Textures with peripheral [c] are often observed in rocks of low grade conditions and based on the postulated temperature dependence of <a> slip systems, it was assumed that (c)<a> may operate readily at low temperature conditions. The expectation that (c)<a> is an easy slip system in quartz relies on studies which actually did not demonstrate the existence of (c)<a> as an easy slip system. The interpretations of the activity of (c)<a>, and hence the contribution to strain are based on the presence of deformation lamellae as well as macroscopic sample features, produced in experiments conducted in most pasts at extremely high differential stresses (e.g. Christie et al. ,1964; Heard & Carter, 1968; Baeta & Ashbee, 1969; Christie & Ardell, 1974; AveLallement & Carter, 1971). Despite the assumption that deformation lamellae represent slip planes has been revised several times (e.g. McLaren & Hobbs, 1972; White, 1973), they were still frequently referred to as indicative of a specific slip system. There is ample evidence for <a>-slip on {m}, {z} and {pi'} while (c)<a>glide evidences were missing (Christie & Green, 1964; Morrison-Smith et al., 1976; Twiss, 1976; Gapais & White; 1982; McLaren, 1983; Linker et al., 1984) and many studies indicate that (c)<a>-related dislocation systems are not found or are likely of very limited mobility unless deforming by climb (e.g. Trepied & Doukhan, 1978; Doukhan & Trepied, 1979; Trepied et al., 1980; Mainprice et al., 1986; Mainprice & Jaoul, 2009; Morales et al., 2011). It is beyond the scope of this contribution to dissect the literature on quartz slip systems, but given that TEM based studies usually find alternatives to easy (c)<a> glide, we will assume that neither purely pole figure based based studies (Bouchez & Pecher, 1981; Schmid & Casey, 1986, Heilbronner & Tullis, 2002; Kilian et al., 2011) nor models (Lister, 1979) can, despite the intriguing geometry, be necessarily taken as evidence for large

Solid Earth Discuss., doi:10.5194/se-2017-44, 2017
Manuscript under review for journal Solid Earth
Discussion started: 19 May 2017

plastic strains accommodated by (c)-<a> glide. In the case of the origin of B-grains by nucleation and growth or growth of specific fragments produced during microcracking in a high driving force environment (high stress, high dislocation density), the presence of B-domains are not related to the activity of (c)<a>.

4.4 Implications for interpretation based on quartz c-axis data

Often, the primary control in experiments to produce the different dislocation creep regimes was temperature (Hirth & Tullis, 1992) and strain rate, although the strength dependence of the different regimes can also be revealed in experiments with different amount of water (Hirth & Tullis, 1992; Stipp et al., 2006). In nature, microstructural transitions have been documented (Stipp et al., 2002) whereas different recrystallization processes developed over a metamorphic gradient and accordingly a correlation of temperature, respectively recrystallization processes with a specific type of texture was tempting. There are widespread examples of Y-maxima textures in natural quartz mylonites where the recrystallization mechanism is mainly subgrain rotation recrystallization with only minor involvement of GBM (Mancktelow, 1987; Fitz Gerald et al., 2006; Pennacchioni et al., 2010) while in the observation of Stipp et al (2002) Y-domains started to appear in only in the GBM regime. Given our observation of the intensification of the Y-maximum with increasing deformation intensity but roughly isothermal conditions, the observations in nature can more easily be interpreted as a function of total strain instead of temperature and a texture dependency on SGR or GBM. Few studies which have a good control on strain and a similar texture evolution is observed, comparable to the texture evolution in regime 2,3 (Pennacchioni et al., 2010) which is in support of our interpretation. Examples of B-domain textures observed at high temperatures (e.g. Menegon et al., 2011) may not indicate an abnormal activity of (c)<a> but rather a high stress texture forming mechanism similar to NGF as suggested here. With relation to temperature determinations, one should also note that within the presented experiments, a range of c-axis opening angles can be found (Fig.3, 4). The observation that the this angle seems to vary as a function of grain shape may have the potential to add another complexity to the c-axis opening angle thermometer.

The different contributions of grain boundary sliding in each regime, in addition to the formation of new, small grains by growth, dominantly in regime 1, may challenge our understanding of the grains size- stress relation with respect to piezometric applications. Similar indications could be drawn by the grain size – gKAM relation which was documented in the companion paper (Heilbronner & Kilian, this volume).

A method to allow the determination of the kinematic vorticity number W_k are based on the measurements of principal and oblique foliations and using the central c-axis girdle to determine the kinematic reference frame (Wallis, 1995). It has been suggested that those are not applicable to the experimentally deformed BHQ based on the experiments of Heilbronner & Tullis (2006; Xypolias, 2009), since it seems the entire girdle rotated with (local) sample strain. Although the current observations show that the general trend of the outer part of the girdle varies with θ (Table 1), if a sufficiently sharp kernel is used (Fig. 1, Appendix 3), it can be seen that the central part of of the girdle remains roughly perpendicular to the shear plane. Measuring the bulk and oblique foliations in the samples and using the method of Wallis (1995), for regime 1, the same kinematic vorticity number is obtained as calculated from the mechanical data (W_k=0.96). However, that result might be considered as a coincidence because in regime 2 ($0.76_{Wallis}/0.93_{bulk}$) and regime 3 ($0.99_{Wallis}/0.92_{bulk}$) obtained values highly deviate. Additionally, it might be questionable whether an oblique grain shape preferred foliation needs to develop parallel to the ISA or if it might be influenced by the recrystallization mechanisms, especially in regime 1.

Solid Earth Discuss., doi:10.5194/se-2017-44, 2017
Manuscript under review for journal Solid Earth
Discussion started: 19 May 2017

5. Summary & Conclusions

To study the textures of BHQ, deformed in general shear to high strain in regimes 1, 2, and 3, EBSD data scanned at moderate spatial resolution (0.5 and 1 µm step size), were analysed using a number of new methods for combined texture and microstructure analysis.

(1) Texture analysis was carried out for classes of different grain size, shape, long axis alignment and grain kernel average misorientation (gKAM) and the geometry of the pole figure skeleton varies systematically within the grain property parameter space. Average grain properties were displayed in c-axis pole figure space to highlight how grain properties correlate with texture.

(2) The grain kernel average misorientation (gKAM) was introduced as a measure for intragranular deformation intensity.

(3) Separate maps of texture strength as a function of grain properties (size, aspect ratio, long axis trend, gKAM) allow for a quantitative comparison and reveal how the bulk texture strength and volumes of the two most prominent fibres, the B- and Y-fibres, decrease and increase, respectively, during the transition from regime 1 to 3.

(4) Textural neighbourhood relations are visualized on maps showing that grains inside the Y subdomains of regime 3 grains are separated by boundaries with higher and lower <a>-intransparency compared to a random distribution, which can be taken as a result of subgrain rotation recrystallization with an addition of geometrically necessary grain boundary sliding.

(5) A colouring system is introduced to connect information from misorientation axes in the specimen and crystal coordinates. The bulk distribution of misorientation axes is always parallel to the vorticity axis, and coincident with rotations which are dominantly around [c] for Y-grains, in R-grains the distribution of rotation axes consist of superposition compatible with a combination of misorienta-

Solid Earth Discuss., doi:10.5194/se-2017-44, 2017
Manuscript under review for journal Solid Earth
Discussion started: 19 May 2017

tion axes compatible with {m}<a>, {z}<a> and {pi'}<a> derived tilt boundaries. For B-grains, no conclusive preference is found, especially no clear indication of a dominance of (c)<a>.

(6) Calculation of the mean generalized Schmid factor on different <a> slip systems as a function of orientation of the applied stress with respect to the sample, shows that in general shear experiments (c)<a> is less likely to operate compared to slip systems such as {pi'}<a>.

Black Hills Quartzite deformed in general shear shows a texture dominated by the alignment of <a> with the trend of the direction of maximum shear stress and a transition of [c] maximum from peripheral (regime 1) to central directions (regime 3) along a kinked single girdle (regime 2). The transition of texture geometry is accompanied by an increase in texture strength. On the basis of the detailed analysis presented above we propose new interpretations concerning texture formation and texture transition, as well as the relation between c-axis orientation and active slip systems and that between texture and recrystallized grain size.

Of the three dislocation creep regimes, only regime 1 and 3 are considered distinct with regime 2 being transitional. Recrystallization in regime 3 happens by subgrain rotation recrystallization and deformation occurs though dislocation creep with a minor contribution of grain boundary sliding. Porphyroclasts in all regimes deform by dislocation glide and climb.

Texture variation as a function of grain size, grain lengthening, long axis alignment and gKAM indicate that [c] rotates away from the periphery of the pole figure with increasing deformation intensity at the grain scale and this rotation is accompanied with a strengthening of the texture. The increasing texture strength is interpreted as a decreasing contribution of grain boundary sliding and an increasing contribution of dislocation glide and climb.

Since the stress level of the experiments is the only differing parameter and there is not observation of a rotation of [c] towards the periphery of the pole figure, we propose and additional texture forming process which operates most efficiently in the high stress regime, i.e. stress controlled growth of new grains. The texture will be a result of the balance of contributions of dislocation glide on several <a> slip systems with [c] attracted towards a bi-maximum at the centre of the pole figure as a function of strain and new grains formed at the periphery of the pole figure, their amount controlled by the stress level. Grains subsequently grow and deform by dislocation glide and grain boundary sliding. The texture presents a dynamic balance between both processes. The hypothesis that (c)<a> slip is responsible for peripheral [c] maxima, {m}<a> slip for the central Y-maximum and {pi'}/{z}<a> for the symmetrically disposed R-maxima, is too simplistic and our interpretation of the texture evolution opens a new field in the interpretation of naturally produced textures. According to our interpretation, a temperature dependency of quartz textures geometry is of indirect nature while the relative contribution of the two texture forming processes are the controlling factors.

Solid Earth Discuss., doi:10.5194/se-2017-44, 2017
Manuscript under review for journal Solid Earth
Discussion started: 19 May 2017

Tables

Table 1: Variation of c-axis girdle trend within each θ class given in Figure 4. For regime 2, also the trend of the strongest maximum, located at the periphery for <a>, and {r} is given. Angles are clockwise with 0° in the West, shear sense is sinistral.

	θ class 1	θ class 2	θ class 3	θ class4
regime 1	91	74	79	90
regime 2	85 (-10, 121)	67 (-18, 114)	72 (-14, 119)	90 (-8, 123)
regime 3	75	68	72	82

Figure captions

Figure 1: Pole figures of high strain samples of regime 1 to 3. (a) Pole figures for poles to planes c,a,m,r and z from EBSD mappings of sample w1092, w946 and w935. Pole figures oriented with the shear zone boundary (forcing blocks) horizontal, shear sense is sinistral. Maximum density and pole figure J-index, given at left and right top of each pole figure, kernel halfwidth 6°. Contour intervals at 2 times uniform density. (b) Inverse pole figures for selected reference directions: loading direction (“σ_1”), shortening instantaneous stretching axis (ISA_2), major axis direction of the ellipsoid (θ') obtained from total sample strain, shear zone boundary (shzb), parallel to the forcing blocks in the experiments, and the plane -45° to the extending ISA_1. Angles above each plot give the trend of the reference directions, all with inclinations of 90° (in the image plane). Contour intervals at 2 times uniform density.

Figure 2: Orientation maps for samples of regime 1 to 3, w1092, w946 and w935. (a) Inverse pole figure colour-coding using the inferred vorticity axis (= specimen z direction = strain Y-direction) as a reference. colour key for purely rotational point group. (b) Inverse pole figure colour-coding using the ISA_2-45° as a reference direction (indicated at bottom) and a colour key for Laue point group symmetry. Note, for regime 2 and 3 samples, include parts of the single crystal quartz forcing blocks at the top and bottom.

Figure 3: C-axes pole figures for different classes of aspect ratio, grain size and θ. On the left, aspect ratio increases to the right, grain size downwards and son the right, grain long axis trend (θ) in four classes clockwise as indicated by range of angles above pole figures, and aspect ratios increasing downwards. Class limits for each property are at equally spaced quantiles of the entire population. Textures are calculated for grain modal orientations (one orientation per grain). Maximum density and pfJ at top left and top right of each pole figure, number of

Solid Earth Discuss., doi:10.5194/se-2017-44, 2017
Manuscript under review for journal Solid Earth
Discussion started: 19 May 2017

grains within each class at the bottom. Contours at 0.5 times uniform density. Shear zone boundary horizontal, shear sense sinistral, upper hemisphere, equal area projections. The rose diagrams at the bottom show the θ distribution and the corresponding classes. The blue diamond indicates the direction of the long axis of the strain ellipsoid and the red circle the direction of the ISA.

Figure 4: Pole figures <a> and {r} in regime 2. Pole figures are calculated for different classes of aspect ratio, grain size and θ for classes given in Figure 3.

Figure 5: Pole figures of grain size, aspect ratio and axial ratio. Average grain sizer, aspect ratio and axial ratio estimated on the c-axis pole figure for grains smaller 25 µm. Upper hemisphere, equal area projection, greyscale bar indicates the average grain size, aspect ratio and axial ratio. Both, aspect ratio and axial ratio are displayed to separately visualize elongated and round grains.

Figure 6: Pole figures for low and high grain kernel average misorientation. (a) Separate pole figures are calculated using grain modal orientations (1 orientation per grain) and all orientations (1 orientation per pixel), separately for grains with gKAM below and above the median value. Grain size ranges of 1-12 µm (regime 1,2, w1092, w946) and 1-25 µm (regime , w9353) were used. (b) Separate pole figures for grain modal orientations and all orientations for grains with a gKAM below the 0.2 quantile and above the 0.8 quantile. Same grain size ranges a in (a). Maximum density and pfJ given at top left and top right of each pole figure, texture index at bottom left and number of grains or orientations within class at the bottom right. Upper hemisphere, equal area projection, contours at 1 times uniform.

Solid Earth Discuss., doi:10.5194/se-2017-44, 2017
Manuscript under review for journal Solid Earth
Discussion started: 19 May 2017

Figure 7 (landscape): Quantitative comparison of texture index and volumes of texture components. Separate colour maps for texture index, B-fibre and Y-fibre volume as a function of aspect ratio, grain size and θ, calculated for low and high gKAM populations.Fibre volumes are calculated as the volume of the ODF within a 30° radius around a c-axis fibre directed towards the peripheral (B-fibre) and the central c-axis maximum (Y-fibre). Absolute values within each column of colour maps are quantitatively comparable. See text for details.

Figure 8: Slip direction intransparency and misorientation axes at boundaries and low angle boundaries. (a) EBSD map of sample w935 (regime 3) with colour-coded [c] direction (Y-domain = pastel colours, peripheral [c] directions = saturated colours), grain boundaries are colour-coded according to the minimal angle between <a> (ignoring polarity) across a grain boundary. White boundaries are transparent for <a>-slip (if adjacent glide planes are also favourably oriented). colour coding is shown in upper hemisphere, equal area [c] pole figure of 1000 randomly selected orientations. (b) Same area as in (a) with grey value indicating the angular distance of [c] from the periphery, and low angle boundaries (2-9° misorientation angle) colour-coded for the misorientation axis in crystal coordinates. Grain boundaries are not shown for clarity.

Figure 9: Misorientation axes of three texture domains. (a) Map with texture domains determined within an angle of 25° around the orientations forming local maxima in the ODF, colour-coded in red (Y-grains), blue (B-grains), pink (R-grains), green (σ-grains), and yellow (all other grains). On right, from top to bottom pole figures for [c], <a> and {r} showing a subset of poles. (b) colour-coding scheme used for misorientation axis directions (see main text for details). (c) Colouring used for crystal directions, rotation axes (assuming pure tilt boundaries) are indicated for some slip systems. (d) Misorientation axes obtained for low angle boundaries (misorientation angles of 2-9°) from grains in the Y-, B- or R-texture component. Misorientation axes are plotted with density contours at

Solid Earth Discuss., doi:10.5194/se-2017-44, 2017
Manuscript under review for journal Solid Earth
Discussion started: 19 May 2017

Solid Earth Discussions
Open Access

steps of 1 times uniform. Point plots are from randomly drawn subsets. Note that directions of highest density in specimen coordinates do not always coincide with the the direction of highest densities in crystal coordinates (e.g. for the R-grains).

Figure 10: Average, generalized Schmid factors (Sf). Sfs are shown for different slip systems (or combinations of slip systems) as a function of the orientation of the stress tensor. A Sf is calculated for the modal orientations of all grains (top) and for every orientation within a map (bottom). The mean Sf is plotted as a function of the direction of $\sigma_{1.}$. On the x-axis, 0° corresponds to a $\sigma_{1.}$ direction of 45° with respect to the shear plane, negative and positive angles correspond to synthetic or antithetic rotations of σ_1 directions.

Solid Earth Discuss., doi:10.5194/se-2017-44, 2017
Manuscript under review for journal Solid Earth
Discussion started: 19 May 2017

Appendix

EBSD data processing

Single mis-indexed pixels have been deleted and reconstructed together with single non-indexed pixels. Subsequently, non-indexed areas not thicker than two pixels wide along grain boundaries were filled during noise removal using a half-quadratic filter (Bergmann et al, 2015). The procedure was adjusted to be edge preserving for continuous boundaries above 1.3° misorientation angle. Grains are calculated using the segmentation algorithm implemented in the mtex tool-box (Bachman, 2011) with a threshold of 10° boundary misorientation angle using the point group 622 and transforming the grain mean orientation back into trigonal point group 321. This procedure avoids Dauphiné twin boundaries (60° rotation around [c]) being erroneously identified as grain boundaries but the main advantage is that the mean orientation of the hexagonal grain represents the modal orientation of the trigonal grain (representing the orientation of the twinned domain occupying the largest area fraction of the grain). The segmentation procedure yields identical results to segmenting grain maintaining the trigonal symmetry and merging grains with boundaries obeying the Dauphiné twin relation ship within a 3° angular interval between the twinning misorientation and the measured grain boundary misorientation (Note this angle refers to the angle between the (mis)orientation and the twinning twinning rotation and hence is always larger or equal to the error allowed for the twinning axis or twinning angle). The latter procedure has the disadvantage that it will not produce a meaningful average grain orientation, while the former is also computationally less expensive.

Texture calculations

Contoured pole figures and inverse pole figures are calculated from the orientation distribution functions (ODF). The ODF was calculated for either all measurements (area weighted) or the grain modal orientations (number weighted or in

Solid Earth Discuss., doi:10.5194/se-2017-44, 2017
Manuscript under review for journal Solid Earth
Discussion started: 19 May 2017

some terminology referred to as one-point-per grain). In case of ODF calculations, the de la ValeePoussin kernel was used. The kernel width was either fixed or estimated using the Kullback-Leibler cross validation implementation in Mtex. Estimated kernel half widths are between 7-14°.

The strength of individual pole figures is given by the maximum of the density distribution and by the pole figure J-index (pfJ, L2-norm of the density distribution on the sphere) as defined by Mainprice et al. (2014) which is more suitable for multi-modal distributions. A uniform pole figure will have a pfJ of 1. When comparing pfJ values of different crystal directions the respective multiplicity (c=2, a=3, m,r,z=6) has to be taken into account.

gKAM

In order to access how much of internal deformation in the sense of a change of orientation within a grain is present, the misorientation to the grain mean orientation can be colour-coded (Fig. A1,a,d). For this purpose, twinning is ignored and an inverse pole figure colour-coding is chosen in such a way that the mean crystal direction coincides with the mean orientation times the white centre of in the inverse pole figure. Misorientations which relate to misorientation angles up to 30° are displayed. In order to inspect the misorientation density inside a grain, imposed by the number and the misorientation angle of low angle boundaries, we use a measure based on the kernel average misorientation (KAM) and the size of the grain. Calculation of the KAM is performed using noise-reduced data (Fig. 2 b,e), since the orientation noise of conventional EBSD renders most KAM information ambiguous. The KAM is the average misorientation angle over a kernel computed for each measurement point. Misorientation angles above a threshold of 8° were ignored. The grain averaged KAM (gKAM) was computed as the KAM divided by the number of indexed pixels for each grain (Fig. 2c,f). The size of the kernel was individually chosen to be of the order 3 or 4, which compares to a 24 or 40 pixel neighbourhood such that grains without any substructures but different grain size maintain an identical gKAM and any grain size dependency is sup-

Solid Earth Discuss., doi:10.5194/se-2017-44, 2017
Manuscript under review for journal Solid Earth
Discussion started: 19 May 2017

pressed as best as possible. In noise free data, the magnitude of the gKAM is a measure of the low angle boundary density and hence an indirect measure for how much grains deformed during dislocation creep. An advantage over the grain orientation spread (GOS) is that it will not be influenced by interior high angle boundaries or twins, however, the gKAM does not measure continuous lattice bending.

Figure captions for appendix figures

Figure A1

Explanation of the gKAM: Crops of EBSD maps of 0.25 and 1 µm step size showing (a,d) the misorientation to the mean orientation within a tightly confined colour range after noise removal. (b,e) Kernel average misorientation (KAM) of 3rd order (24 pixel neighbourhood) of boundaries below 8° misorientation angle. (c,f) grain averaged KAM as defined by the sum of the KAM of all pixels within a grain divided by the number of pixels. The gkAM can be seen as a measure of misorientation density within a grain, imposed by the frequency and the angle of low angle boundaries. The absolute magnitude of the gKAM will depend on the order of the KAM and the step size and the noise level.

Figure A2

Distribution of angles between adjacent <a> directions across a grain boundaries in regime 3. Histogram for grains within the Y-domains (contained within a 40° cone for the c-axis directions), out side this domain and for interdomainal boundaries. Stippled line shows the distribution expected for a uniformly textured aggregate.

Figure A3

Solid Earth Discuss., doi:10.5194/se-2017-44, 2017
Manuscript under review for journal Solid Earth
Discussion started: 19 May 2017

Solid Earth
Discussions

Pole figures of c,a,r from regime 1,2 and 3 entire sample and directions corresponding to the orientation modes found in the ODF with densities >3. Numbers correspond to the poles obtained from modes in with decreasing density. Positions of highest densities on a pole figure do not need to exactly coincide with poles to the modes. (a,b,c) are upper hemisphere, equal area projections. Note Bi-modal character of [c] distributions in the centre of the pole figure in regime 2 and 3.

Figure A4

Misorientation axes for regime 1, 2, and 3. colour coding and types of plots identical to Figure 9 in the main text, except that misorientation axes for all texture components are shown.

Solid Earth Discuss., doi:10.5194/se-2017-44, 2017
Manuscript under review for journal Solid Earth
Discussion started: 19 May 2017

6. References

Ardell, a. J., J. M. Christie, and J. W. McCormick (1974), Dislocation images in quartz and determination of burgers vectors, Philos. Mag., 29(6), 1399–1411.

Avelallemant, H., and N. Carter (1971), Pressure dependence of quartz deformation lamellae orientations, American Journal of Science, 270(3), 218-235.

Bachmann, F., R. Hielscher, and H. Schaeben (2011), Grain Detection From 2D and 3D EBSD Data-Specification of The Mtex Algorithm, Ultramicroscopy, 111(12), 1720–1733, Doi:10.1016/J.Ultramic.2011.08.002.

Baeta, R., and K. Ashbee (1969), Slip Systems in Quartz .2. Interpretation, American Mineralogist, 54(11-1), 1574–1582.

Bergmann, R., R. H. Chan, R. Hielscher, J. Persch, and G. Steidl (2016), Restoration of Manifold-Valued Images by Half-Quadratic Minimization, Inverse Problems and Imaging, 10 (2), 281–304, Doi:10.3934/Ipi.2016001.

Blacic, J. (1975), Plastic-Deformation Mechanisms in Quartz - Effect of Water, Tectonophysics, 27(3), 271–294.

Bouchez, J. L., and a. Pecher (1981), The Himalayan Main Central Thrust Pile and its Quartz-Rich Tectonites in Central Nepal, Tectonophysics, 78(1-4), 23–50.

Cahn, J. W., and Y. Mishin (2009), Recrystallization Initiated by Low-Temperature Grain Boundary Motion Coupled to Stress, Int. J. Mater. Res., 100(4), 510–515, Doi:10.3139/146.110066.

Christie, J., and H. W. Green (1964), Several New Slipsystems in Quartz, Eos Trans.Agu, 45, P. 102.

Christie, J. M., D. T. Griggs, and N. L. Carter (1964), Experimental Evidence of Basal Slip in Quartz, J. Geol., 72(6), 734–&.

DellAngelo, L., and J. Tullis (1989), Fabric Development in Experimentally Sheared Quartzites, Tectonophysics, 169(1-3), 1–21.

Den Brok, S.WJ., Spiers, C.J. (1991) Experimental evidence for water weakening of quartzite by microracking plus solution-precipitation creep. Journal of the Geological Society, London, 148, 541-548.

Doukhan, J. C., and L. Trepied (1979), Plasticity of Quartz - Crystallographic Models and TEM Observations, B Mineral, 102(2-3), 138–147.

Fitz Gerald, J., J. Boland, A. McLaren, A. Ord, and B. Hobbs (1991), Microstructures in Water-Weakened Single-Crystals of Quartz, Journal of Geophysical Research-Solid Earth and Planets, 96(B2), 2139–2155.

Fitz Gerald, J., N. Mancktelow, G. Pennacchioni, and K. Kunze (2006), Ultrafine-grained Quartz Mylonites From High-Grade Shear Zones: Evidence for Strong Dry Middle to Lower Crust, Geology, 34(5), 369–372, Doi: 10.1130/G22099.1.

Fossen, H., and B. Tikoff (1993), The Deformation Matrix for Simultaneous Simple Shearing, Pure Shearing and Volume Change, and Its Application to Transpression-Transtension Tectonics, Journal of Structural Geology, 15(3-5), 413–422.

Gapais, D., and S. White (1982), Ductile Shear Bands in a Naturally Deformed Quartzite, Textures and Microstructures, 5, 1–17.

Gleason, G. C., J. Tullis, and F. Heidelbach (1993), The Role of Dynamic Recrystallization in the Development of Lattice Preferred Orientations in Experimentally Deformed Quartz Aggregates, J. Struct. Geol., 15(9-10), 1145–1168.

Heard, H. C., and N. L. Carter (1968), Experimentally Induced Natural Intragranular Flow in Quartz and Quartzite, Am. J. Sci., 266(1), 1–17.

Heilbronner, R., and J. Tullis (2002), The Effect of Static Annealing On Microstructures and Crystallographic Preferred Orientations of Quartzites Experimentally Deformed in Axial Compression and Shear, in Deformation Mechanisms, Rheology and Tectonics: Current Status and Future Perspectives, Geological Society Special Publication, Vol. 200, edited by DeMeer, S. and Drury, M. and DeBresser, J. H. and Pennock, G., 191–218 Doi:10.1144/Gsl.Sp.2001.200.01.12

Heilbronner, R., and J. Tullis (2006), Evolution of C Axis Pole Figures and Grain Size During Dynamic Recrystallization: Results From Experimentally Sheared Quartzite, Journal of Geophysical Research-Solid Earth, 111(B10), B10,202, Doi:10.1029/2005jb004194.

Hippertt, J. (1994), Microstructures and C-Axis Fabrics Indicative of Quartz Dissolution in Sheared Quartzites and Phyllonites, Tectonophysics, 229(3-4), 141–163.

Hippertt, J., and M. Egydiosilva (1996), New Polygonal Grains Formed by Dissolution-Redeposition in Quartz Mylonite, J. Struct. Geol., 18(11), 1345–1352.

Hirth, G., and J. Tullis (1992), Dislocation Creep Regimes in Quartz Aggregates, Journal of Structural Geology, 14(2), 145–159.

Hobbs, B. E. (1968), Recrystallization of Single Crystals of Quartz, Tectonophysics, 6(5), 353–&.

Hobbs, B. E. (1985), The Geological Significance of Microfabric, in Preferred Orientation in Deformed Metals and Rocks, edited by Wenk, H.R. 463-489, Academic Press, New York.

Jaoul, O., J. Tullis, and a. Kronen- Berg (1984), The Effect of Varying Water Contents On The Creep-Behavior of Heavitree Quartzite, Journal of Geophysical Research, 89 (NB6), 4298–4312, Doi:10.1029/Jb089ib06p04298.

Kilian, R., R. Heilbronner, and H. Stunitz (2011), Quartz Grain Size Reduction in a Granitoid Rock and The Transition From Dislocation to Diffusion Creep, J. Struct. Geol., 33(8), 1265–1284, Doi:10.1016/J.Jsg.2011.05.004.

Solid Earth Discuss., doi:10.5194/se-2017-44, 2017
Manuscript under review for journal Solid Earth
Discussion started: 19 May 2017

Kilian, R., R. Heilbronner, I. Holyoke, Caleb W., a. K. Kronenberg, and H. Stunitz (2016), Dislocation Creep of Dry Quartz, J. Geophys. Res.-Solid Earth, 121(5), 3278–3299, Doi:10.1002/2015jb012771.

Kjoll, H. J., G. Viola, L. Menegon, and B. E. Sorensen (2015), Brittle-Viscous Deformation of Vein Quartz Under Fluid-Rich Lower Greenschist Facies Conditions, Solid Earth, 6(2), 681–699, Doi:10.5194/Se-6-681-2015.

Kottada, R. S., and a. H. Chokshi (2007), Grain Boundary Sliding During Diffusion and Dislocation Creep in a Mg-0.7 Pct Al Alloy, Metallurgical and Materials Transactions a- Physical Metallurgy and Materials Science, 38a(8), 1743–1749, Doi: 10.1007/S11661-007-9190-X.

Kronenberg, a., and J. Tullis (1984), Flow Strengths of Quartz Aggregates - Grain-Size and Pressure Effects Due to Hydrolytic Weakening, Journal of Geophysical Research, 89 (NB6), 4281–4297.

Kruhl, J.H., 1998. Reply: prism- and basal-plane parallel subgrain boundaries in quartz: a microstructural geothermobarometer. J. Metamorph. Geol. 16, 142-146.

Law, R. D. (2014), Deformation Thermometry Based On Quartz C-Axis Fabrics and Recrystallization Microstructures: a Review, J. Struct. Geol., 66, 129–161, Doi:10.1016/J.Jsg.2014.05.023.

Law, R. D., S. M. Schmid, and J. Wheeler (1990), Simple Shear Deformation and Quartz Crystallographic Fabrics - a Possible Natural Example From The Torridon Area of Nw Scotland, J. Struct. Geol., 12(1), 29–45.

Linker, M. F., S. H. Kirby, a. Ord, and J. M. Christie (1984), Effects of Compression Direction On The Plasticity and Rheology of Hydrolytically Weakened Synthetic Quartz Crystals At Atmospheric-Pressure, J. Geophys. Res., 89(Nb6), 4241–4255.

Lister, G., and U. Dornsiepen (1982), Fabric Transitions in The Saxony Granulite Terrain, Journal of Structural Geology, 4(1), 81–92.

Lister, G. S. (1979), Fabric Transitions in Plastically Deformed Quartzites - Competition Between Basal, Prism and Rhomb Systems, B Mineral, 102(2-3), 232–241.

Mainprice, D., and O. Jaoul (2009), a Transmission Electron Microscopy Study of Experimentally Deformed Quartzite With Different Degrees of Doping, Physics of The Earth and Planetary Interiors, 172(1-2), 55–66, Doi:10.1016/J.Pepi.2008.07.009.

Mainprice, D., J. L. Bouchez, P. Blumenfeld, and J. M. Tubia (1986), Dominant-C Slip in Naturally Deformed Quartz - Implications for Dramatic Plastic Softening At High-Temperature, Geology, 14(10), 819–822.

Mainprice, D., F. Bachmann, R. Hielscher, and H. Schaeben (2015), Descriptive Tools for The Analysis of Texture Projects With Large Datasets Using Mtex: Strength, Symmetry and Components, in Rock Deformation From Field, Experiments and Theory: a Volume in Honour of Ernie Rutter, Geological Society Special Publication, Vol. 409, Edited by Faulkner, D and Mariani, E and Mecklenburgh, J, Pp. 251–271, Doi:10.1144/Sp409.8, Conference On Rock Deformation From Field, Experiments and Theory in Honour of Ernie Rutter, Geol Soc London, London, England, May 30-31, 2012.

Mancktelow, N., and G. Pennacchioni (2004), The Influence of Grain Boundary Fluids On The Microstructure of Quartz-Feldspar Mylonites, Journal of Structural Geology, 26 (1), 47–69, Doi:10.1016/S0191-8141(03)00081-6.

Mancktelow, N. S. (1987), Atypical Textures in Quartz Veins From The Simplon Fault Zone, J. Struct. Geol., 9(8), 995–1005.

McLaren, a. C., and B. E. Hobbs (1972), in Flow and Fracture of Rocks, Vol. Geophysical Monograph 16, Chap. Transmission Electron Microscope Investigation of Some Naturally Deformed Quartzites, Pp. 55–66, American Geophysical Union.

McLaren, a. C., R. F. Cook, S. T. Hyde, and R. C. Tobin (1983), The Mechanisms of The Formation and Growth of Water Bubbles and Associated Dislocation Loops in Synthetic Quartz, Phys. Chem. Miner., 9(2), 79–94.

Menegon, L., G. Pennacchioni, R. Heilbronner, and L. Pittarello (2008), Evolution of Quartz Microstructure and C-Axis Crystallographic Preferred Orientation within Ductilely Deformed Granitoids (Arolla Unit, Western Alps), J. Struct. Geol., 30(11), 1332–1347, Doi:10.1016/J.Jsg.2008.07.007.

Morales, L. F. G., D. Mainprice, G. E. Lloyd, and R. D. Law (2011), Crystal Fabric Development and Slip Systems in a Quartz Mylonite: An Approach Via Transmission Electron Microscopy and Viscoplastic Self-Consistent Modelling, in Deformation Mechanisms, Rheology and Tectonics: Microstructures, Mechanics and Anisotropy, Geological Society Special Publication, Vol. 360, Edited by Prior, D. J. and Rutter, E. H. and Tatham, D. J., Pp. 151–174, Geological Soc Publishing House, Doi:10.1144/Sp360.9.

Morgan, S.S., Law, R.D., 2004. Unusual transition in quartzite dislocation creep regimes and crystal slip systems in the aureole of the EJB pluton, California: a case for anhydrous conditions created by decarbonation of adjacent marbles. Tectonophysics 384, 209-231.

Morrison-Smith, D. J., M. S. Paterson, and B. E. Hobbs (1976), Electron-Microscope Study of Plastic-Deformation in Single-Crystals of Synthetic Quartz, Tectonophysics, 33(1-2), 43–79.

Paterson, M. (1989), The Interaction of Water With Quartz and Its Influence in Dislocation Flow—An Overview, Pp. 107–142, Rheology of Solids and of The Earth, Oxford Science Publications, Oxford.

Pennacchioni, G., L. Menegon, B. Leiss, F. Nestola, and G. Bromiley (2010), Development of Crystallographic Preferred Orientation and Microstructure During Plastic Deformation of Natural Coarse-Grained Quartz Veins, Journal of Geophysical Research-Solid Earth, 115, Doi: 10.1029/2010jb007674.

Schmid, S., and M. Casey (1986), Complete Fabric Analysis of Some Commonly Observed Quartz C-Axis Patterns, Geophysical Monograph, Vol. 36, Pp. 263–286, American Geophysical Union.

Schmid, S., R. Panozzo, and S. Bauer (1987), Simple Shear Experiments On Calcite Rocks - Rheology and Microfabric, Journal of Structural Geology, 9(5-6), 747–778.

Sullivan, W.A., Beane, R.J., 2010. Asymmetrical quartz crystallographic fabrics formed during constructional deformation. J. Struct. Geol. 32, 1430-1443.

Stipp, M., and K. Kunze (2008), Dynamic Recrystallization Near The Brittle-Plastic Transition in Naturally and Experimentally Deformed Quartz Aggregates, Tectonophysics, 448 (1-4), 77–97, Doi:10.1016/J.Tecto.2007.11.041.

Stipp, M., H. Stunitz, R. Heilbronner, and S. Schmid (2002), The Eastern Tonale Fault Zone: a ’natural Laboratory’ for Crystal Plastic Deformation of Quartz Over a Temperature Range From 250 to 700 Degrees C, Journal of Structural Geology, 24(12), 1861–1884.

Stipp, M., J. Tullis, and H. Behrens (2006), Effect of Water On The Dislocation Creep Microstructure and Flow Stress of Quartz and Implications for The Recrystallized Grain Size Piezometer, Journal of Geophysical Research-Solid Earth, 111 (B4), Doi:Doi 10.1029/2005jb003852.

Stunitz, H., a. Thust, R. Heilbronner, H. Behrens, R. Kilian, a. Tarantola, and J. D. F. Gerald (2017), Wa- Ter Redistribution in Experimentally Deformed Natural Milky Quartz Single Crystals-Implications for H2o-Weakening Processes, J. Geophys. Res.-Solid Earth, 122(2), 866–894, Doi:10.1002/2016jb013533.

Thigpen, J.R., Law, R.D., Lloyd, G.E., Brown, S.J., Cook, B., 2010. Deformation temperatures, vorticity of flow and strain symmetry in the Loch Eriboll mylonites, NW Scotland: implications for the kinematic and structural evolution of the northernmost Moine thrust zone. In: Law, R.D., Butler, R.W.H., Holdsworth, R., Krabbendam, M., Strachan, R.A. (Eds.), Continental Tectonics and Mountain Building e The Legacy of Peach and Horne, Geological Society of London, Special Publications, vol. 335, pp. 623-662 doi:10.144/SP335.26.

Toy, V. G., D. J. Prior, and R. J. Norris (2008), Quartz Fabrics in The Alpine Fault Mylonites: Influence of Pre-Existing Preferred Orientations On Fabric Development During Progressive Uplift, J. Struct. Geol., 30(5), 602–621, Doi:10.1016/J.Jsg.2008.01.001.

Trepied, L., and J. C. Doukhan (1978), Dissociated Alpha- Dislocations in Quartz - Influence On Plastic-Deformation, Phys. Status Solidi a-Appl. Res., 49(2), 713– 724.

Trepied, L., J. Doukhan, and J. Paquet (1980), Sub- Grain Boundaries in Quartz - Theoretical-Analysis and Microscopic Observations, Physics and Chemistry of Minerals, 5(3), 201–218.

Trepmann, C. a., and B. Stoeckhert (2013), Short-Wavelength Undulatory Extinction in Quartz Recording Coseismic Deformation in The Middle Crust - An Experimental Study, Solid Earth, 4(2), 263–276, Doi:10.5194/Se-4-263-2013.

Trepmann, C. a., B. Stockhert, D. Dorner, R. H. Moghadam, M. Kuester, and K. Roeller (2007), Simulating Coseismic Deformation of Quartz in The Middle Crust and Fabric Evolution during Postseismic Stress Relaxation - An Experimental Study, Tectonophysics, 442(1-4), 83–104, Doi:10.1016/J.Tecto.2007.05.005.

Tullis, J. (2002), Deformation of Granitic Rocks: Experimental Studies and Natural Examples, in Plastic Deformation of Minerals and Rocks, Reviews in Mineralogy & Geochemistry, Vol. 51, Edited by Karato, S and Wenk, H.R., Pp. 51–95, Mineralog. Soc. Amer., Doi: 10.2138/Gsrmg.51.1.51, Conference On Plastic Deformation of Minerals and Rocks, Berkeley, Ca, Dec 04-05, 2002.

Solid Earth Discuss., doi:10.5194/se-2017-44, 2017
Manuscript under review for journal Solid Earth
Discussion started: 19 May 2017

Tullis, J., and T. Tullis (1972), Flow and Fracture of Rocks, Chap. Preferred Orientation of Quartz Produced by Mechanical Dauphine Twinning: Thermodynamics and Axial Experiments, Pp. 62–82, 16, Amer. Geophys. Union Monograph.

Tullis, J., J. Christie, and D. Griggs (1973), Microstructures and Preferred Orientations of Experimentally Deformed Quartzites, Geological Society of America Bulletin, 84(1), 297–314.

Twiss, R. J. (1976), Some Planar Deformation Features, Slip Systems, and Submicroscopic Structures in Synthetic Quartz, J. Geol., 84(6), 701–724.

Vernooij, M. G. C., K. Kunze, and B. Den Brok (2006a), 'brittle' Shear Zones in Experimentally Deformed Quartz Single Crystals, J. Struct. Geol., 28(7), 1292–1306, Doi:10.1016/J.Jsg.2006.03.018.

Vernooij, M. G. C., B. Den Brok, and K. Kunze (2006b), Development of Crystallographic Preferred Orientations by Nucleation and Growth of New Grains in Experimentally Deformed Quartz Single Crystals, Tectonophysics, 427(1-4), 35–53, Doi: 10.1016/J.Tecto.2006.06.008.

Wallis, S. (1995), Vorticity Analysis and Recognition of Ductile Extension in The Sambagawa Belt, SW Japan, J. Struct. Geol., 17(8), 1077–1093.

Wenk, H.R. & Christie, J.M. 1991. Comments on the interpretation of deformation textures in rocks. Journal of Structural Geology, 13, 1091-1110.

White, S. (1973), Dislocation-Structures Responsible for Optical Effects in Some Naturally-Deformed Quartzes, J. Mater. Sci., 8(4), 490–499.

Xypolias, R. (2009), Some New Aspects of Kinematic Vorticity Analysis in Naturally Deformed Quartzites, J. Struct. Geol., 31(1), 3–8, Doi:10.1016/J.Jsg.2008.09.009.

Zhang, Y., M. W. Jessell, and B. E. Hobbs (1996), Experimental and Numerical Studies of The Accommodation of Strain Incompatibility On The Grain Scale, Journal of Structural Geology, 18(4), 451–460.

Solid Earth Discuss., doi:10.5194/se-2017-44, 2017
Manuscript under review for journal Solid Earth
Discussion started: 19 May 2017

Solid Earth
Discussions
Open Access

Figure 1

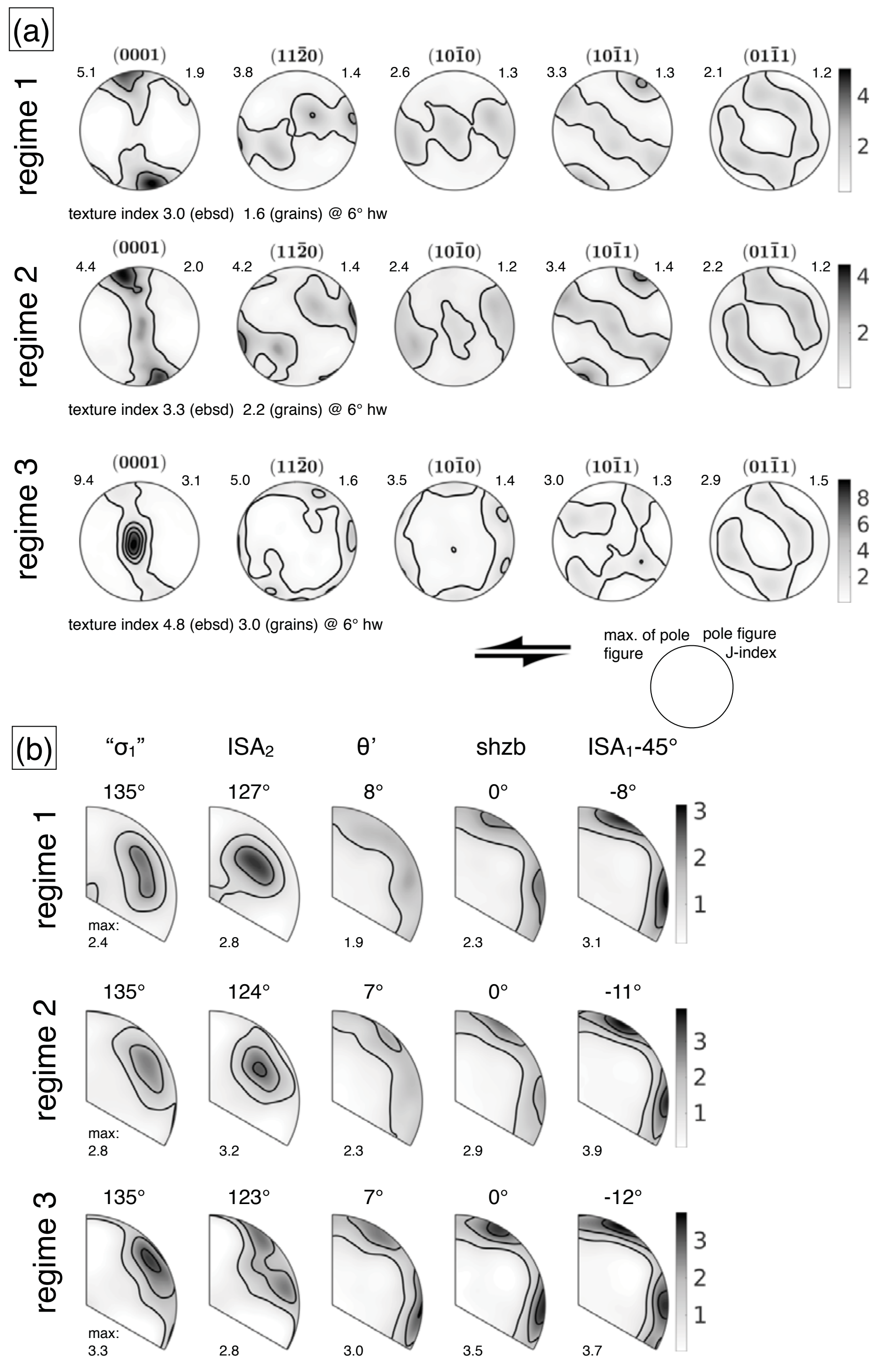

Solid Earth Discuss., doi:10.5194/se-2017-44, 2017
Manuscript under review for journal Solid Earth
Discussion started: 19 May 2017

Figure 2

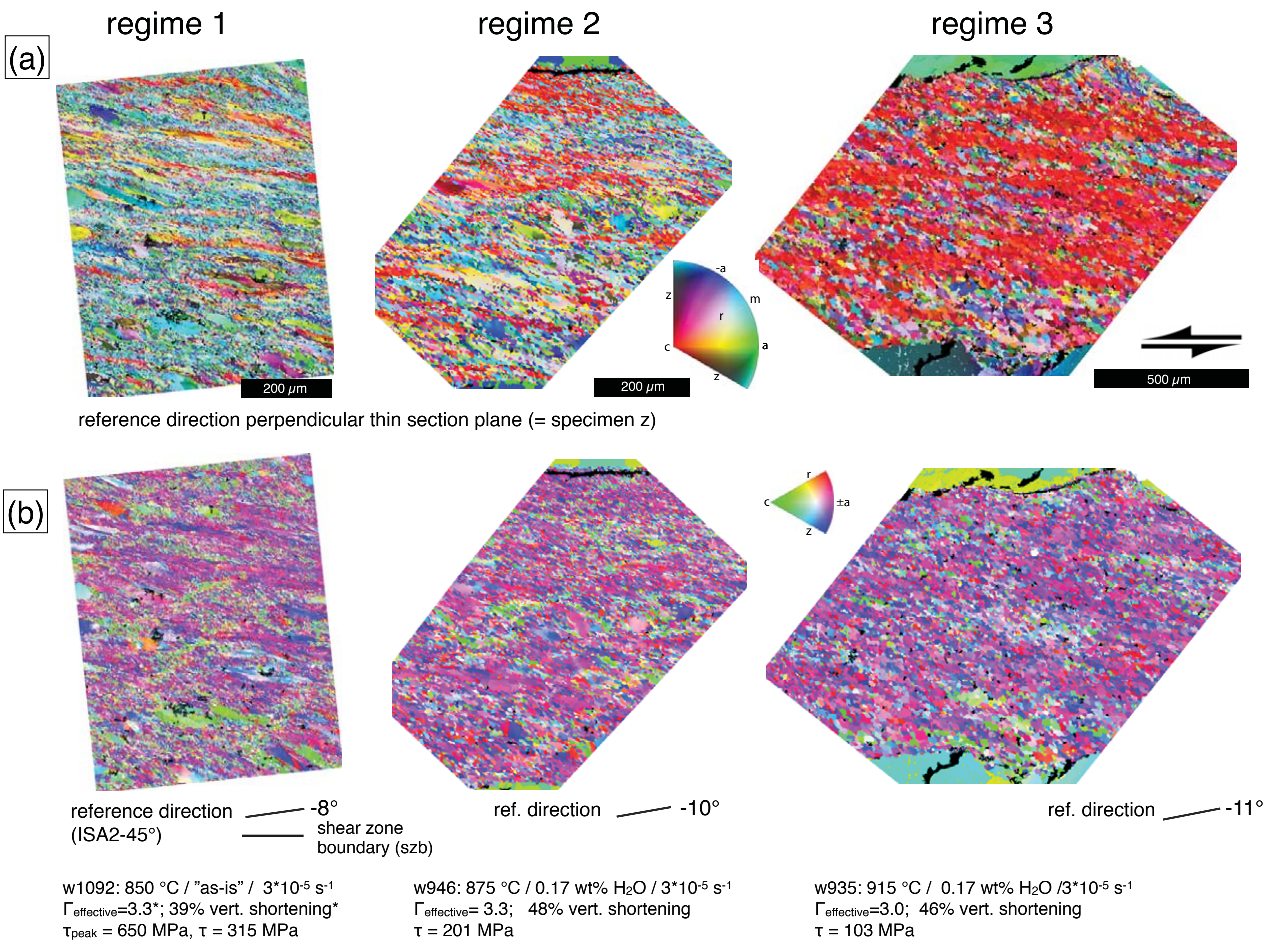

Solid Earth Discuss., doi:10.5194/se-2017-44, 2017
Manuscript under review for journal Solid Earth
Discussion started: 19 May 2017

Figure 3

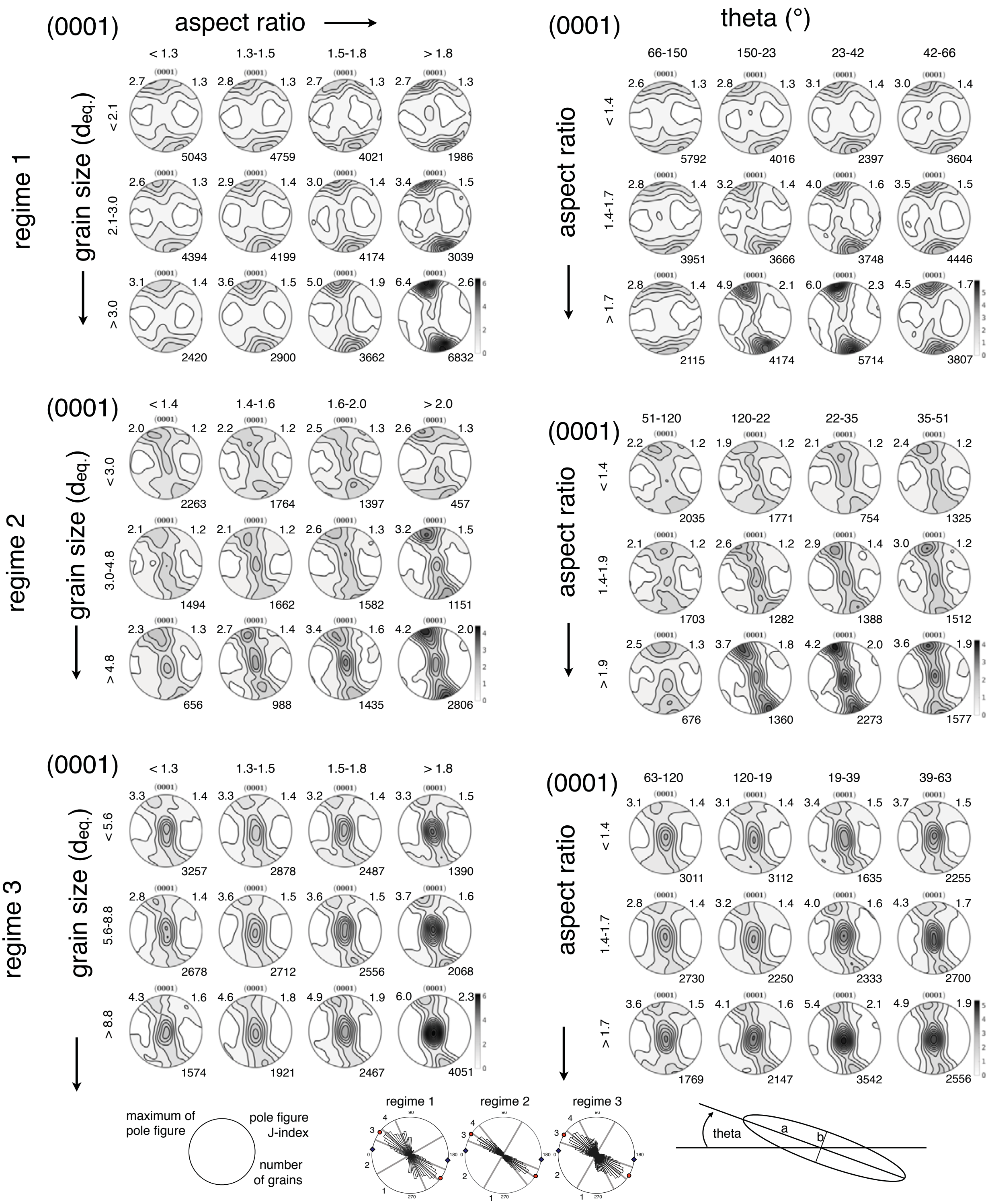

Figure 4

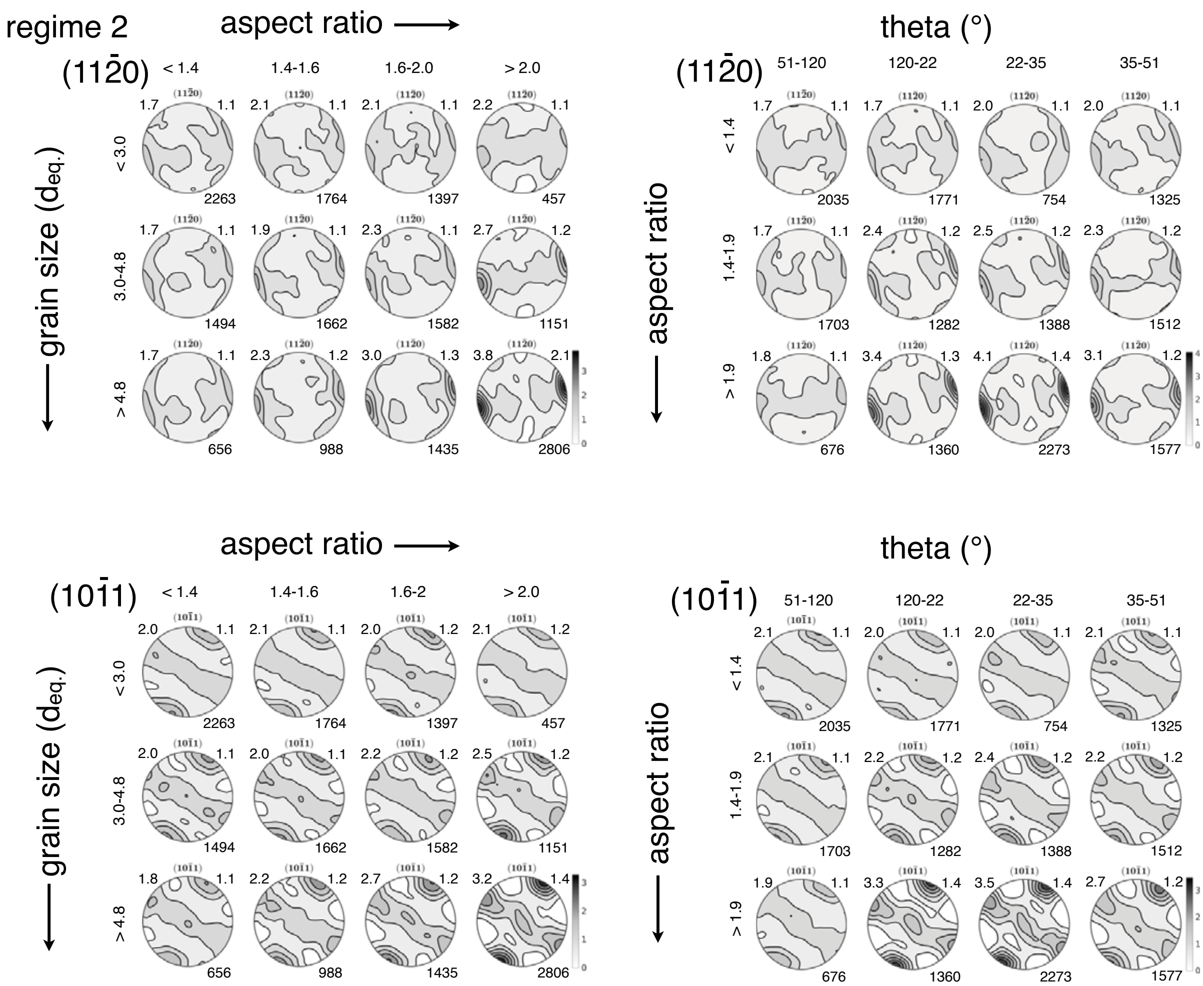
regime 2
aspect ratio
(11$\bar{2}$0)
< 1.4
1.4-1.6
1.6-2.0
> 2.0
grain size (deq.)
< 3.0
3.0-4.8
> 4.8
theta (°)
51-120
120-22
22-35
35-51
aspect ratio
< 1.4
1.4-1.9
> 1.9
(10$\bar{1}$1)
1.6-2

Solid Earth Discuss., doi:10.5194/se-2017-44, 2017
Manuscript under review for journal Solid Earth
Discussion started: 19 May 2017

Solid Earth
Discussions
Open Access

Figure 5

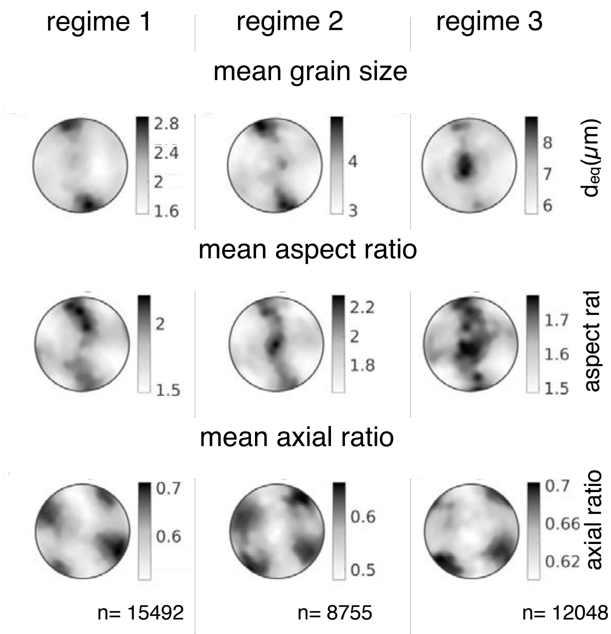

Solid Earth Discuss., doi:10.5194/se-2017-44, 2017
Manuscript under review for journal Solid Earth
Discussion started: 19 May 2017

Solid Earth
Discussions
Open Access
EGU

Figure 6a

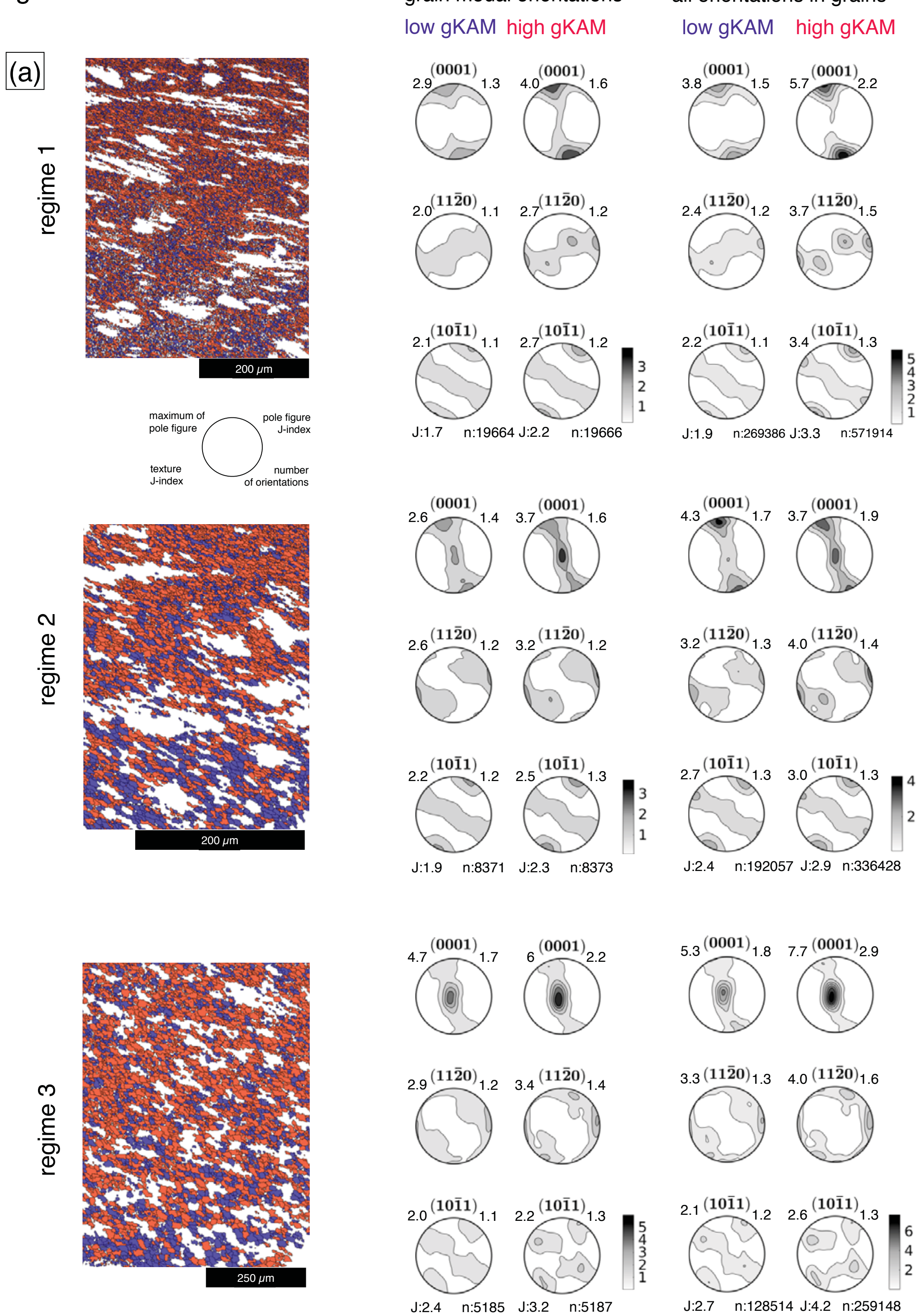

Solid Earth Discuss., doi:10.5194/se-2017-44, 2017
Manuscript under review for journal Solid Earth
Discussion started: 19 May 2017

Figure 6b

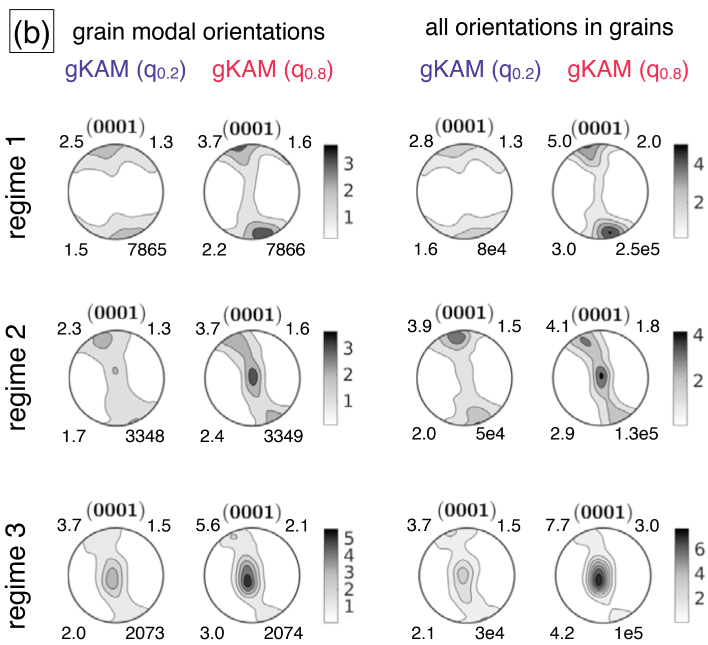

Solid Earth Discuss., doi:10.5194/se-2017-44, 2017
Manuscript under review for journal Solid Earth
Discussion started: 19 May 2017

Figure 7

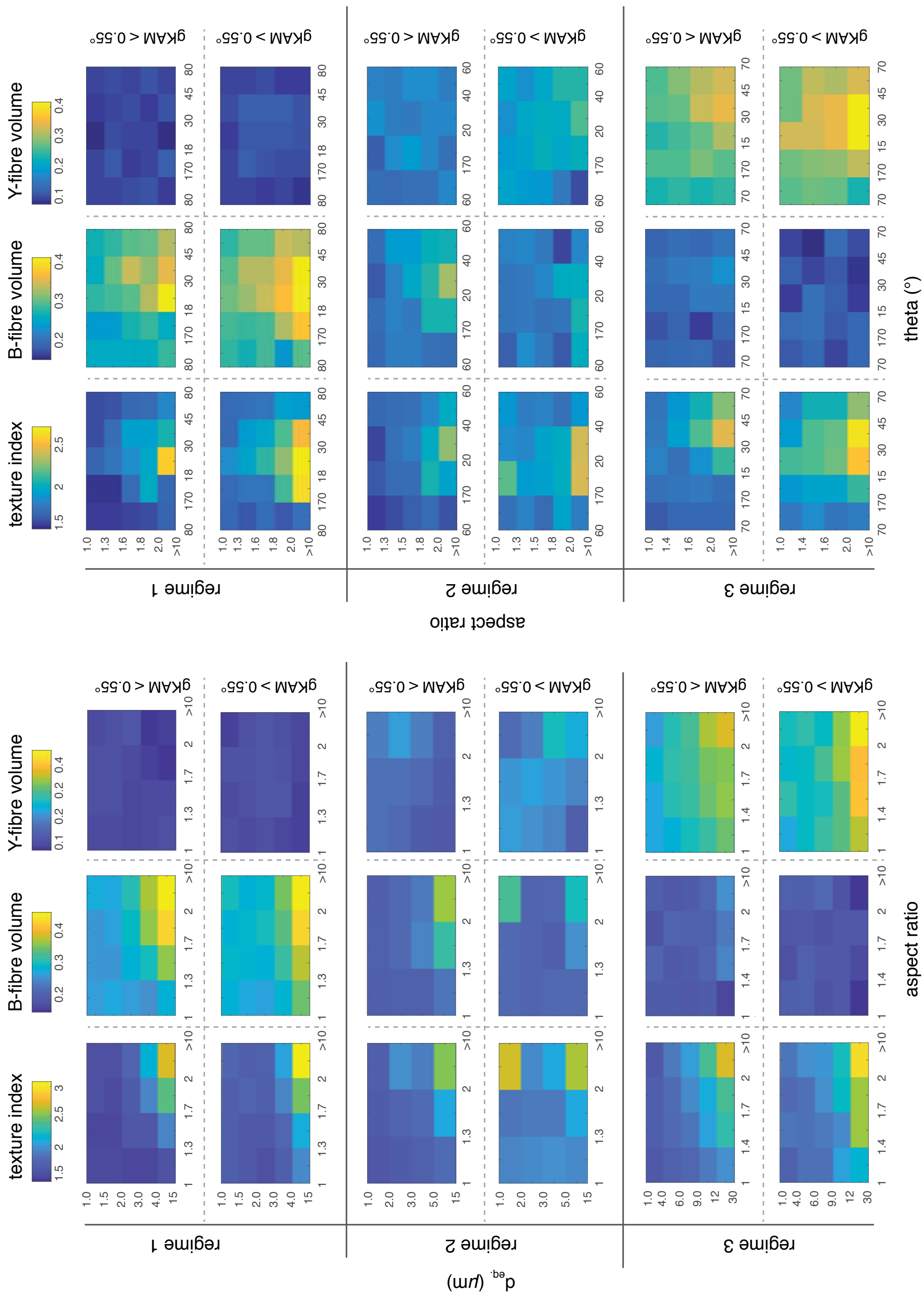

Solid Earth Discuss., doi:10.5194/se-2017-44, 2017
Manuscript under review for journal Solid Earth
Discussion started: 19 May 2017

Solid Earth
Discussions
Open Access

Figure 8

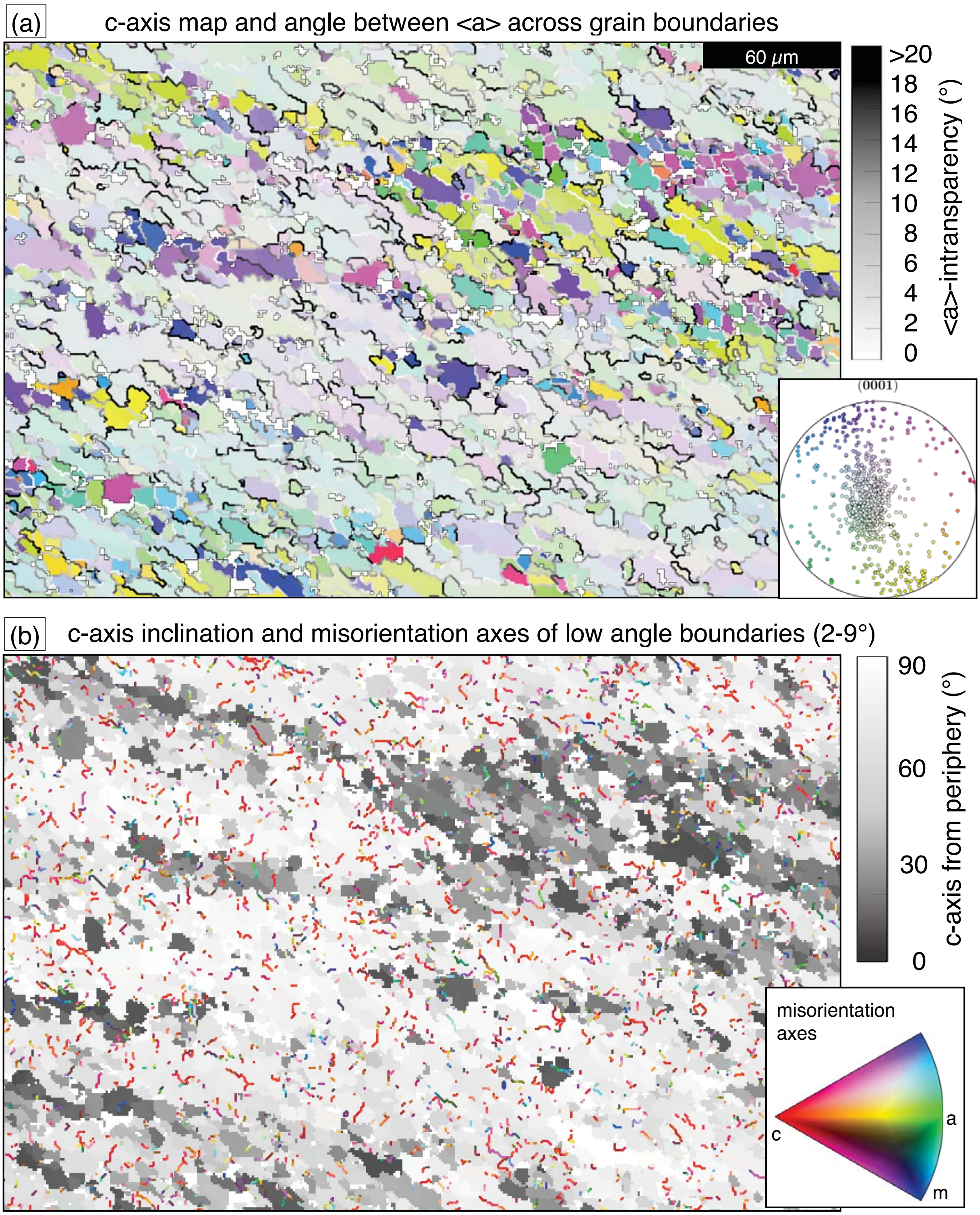

Solid Earth Discuss., doi:10.5194/se-2017-44, 2017
Manuscript under review for journal Solid Earth
Discussion started: 19 May 2017

Solid Earth
Discussions
Open Access

Figure 9

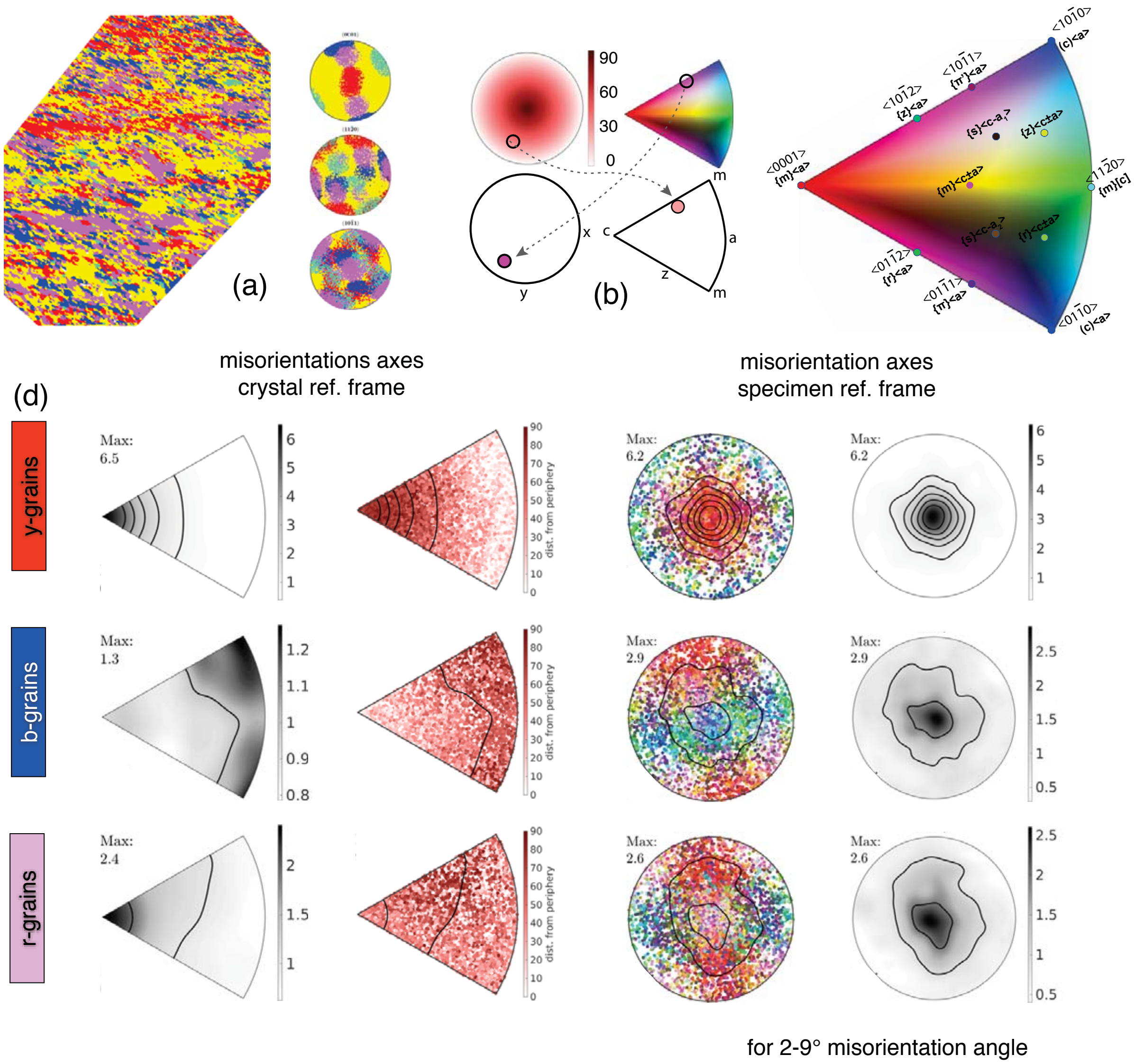

Solid Earth Discuss., doi:10.5194/se-2017-44, 2017
Manuscript under review for journal Solid Earth
Discussion started: 19 May 2017

Solid Earth
Discussions
Open Access

Figure 10

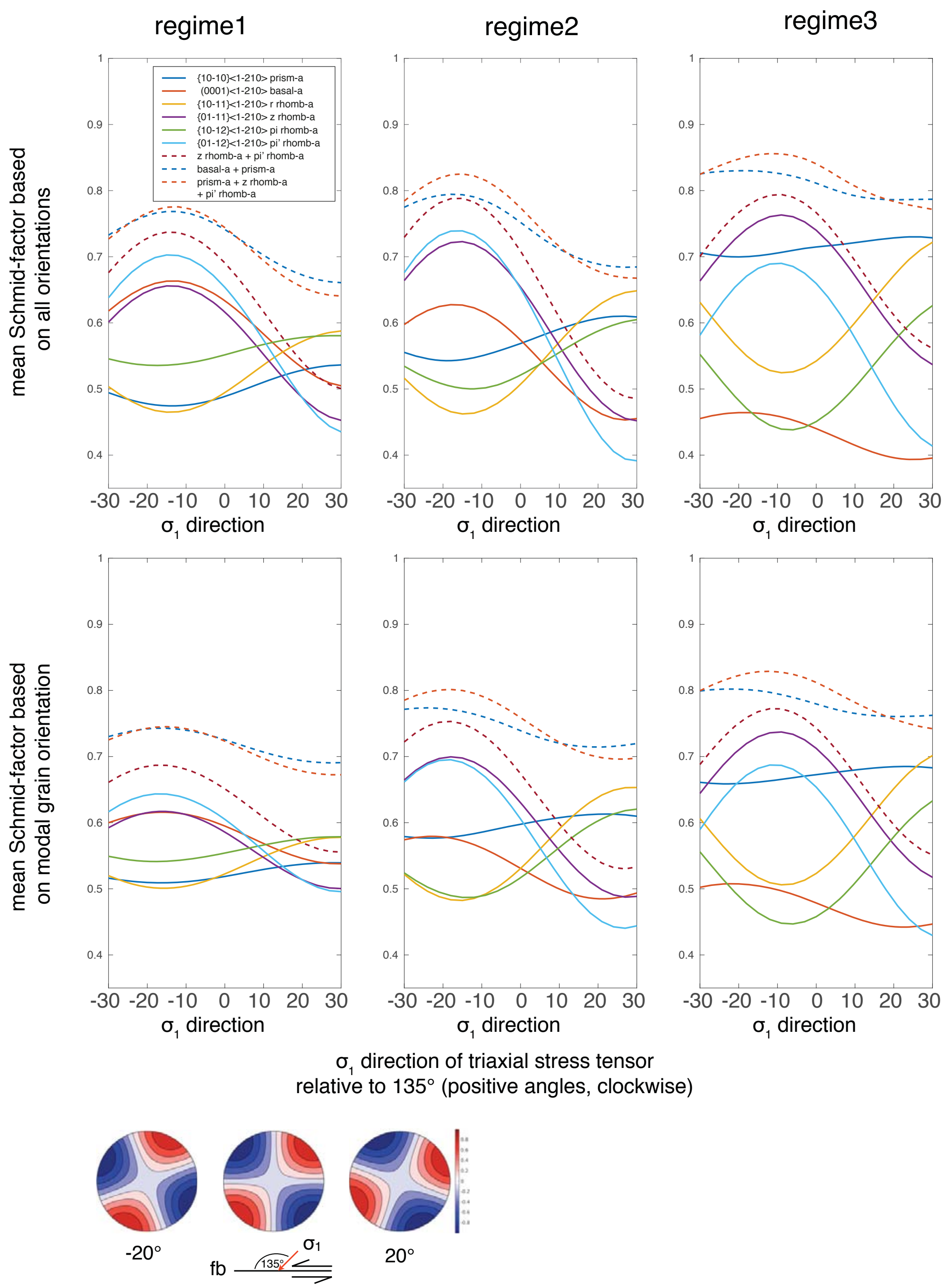

Solid Earth Discuss., doi:10.5194/se-2017-44, 2017
Manuscript under review for journal Solid Earth
Discussion started: 19 May 2017

Appendix Figure A1

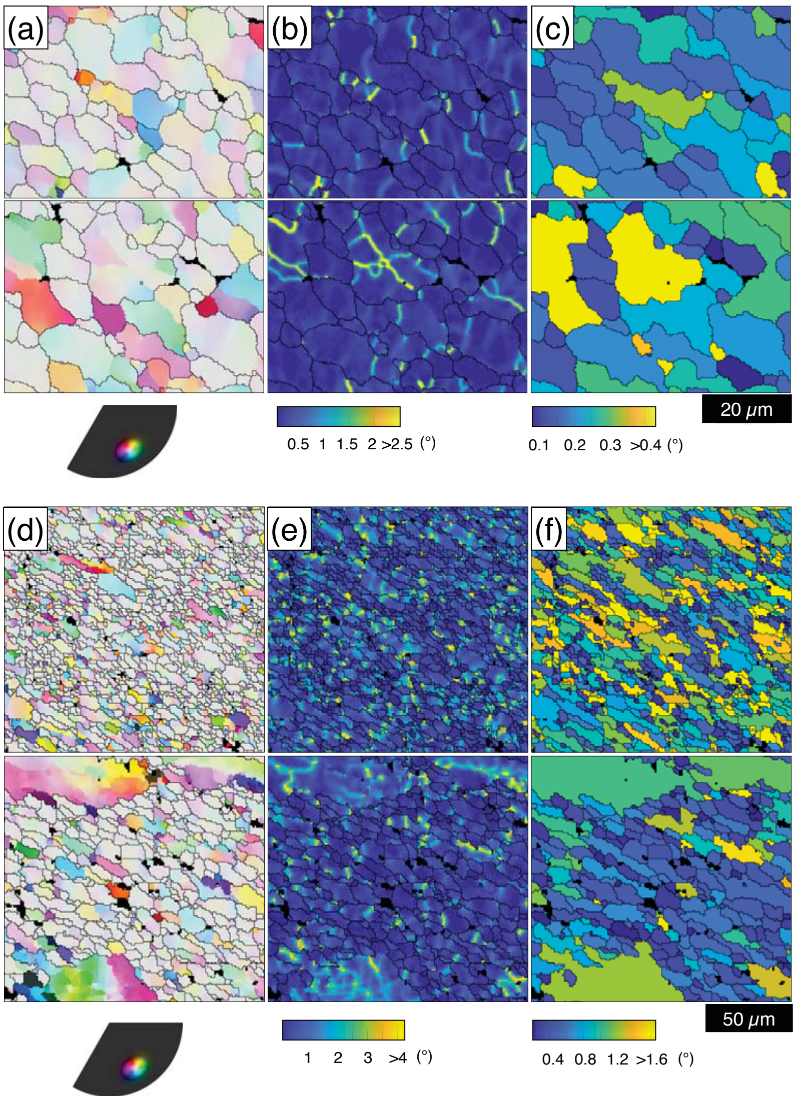

Solid Earth Discuss., doi:10.5194/se-2017-44, 2017
Manuscript under review for journal Solid Earth
Discussion started: 19 May 2017

Appendix Figure A2

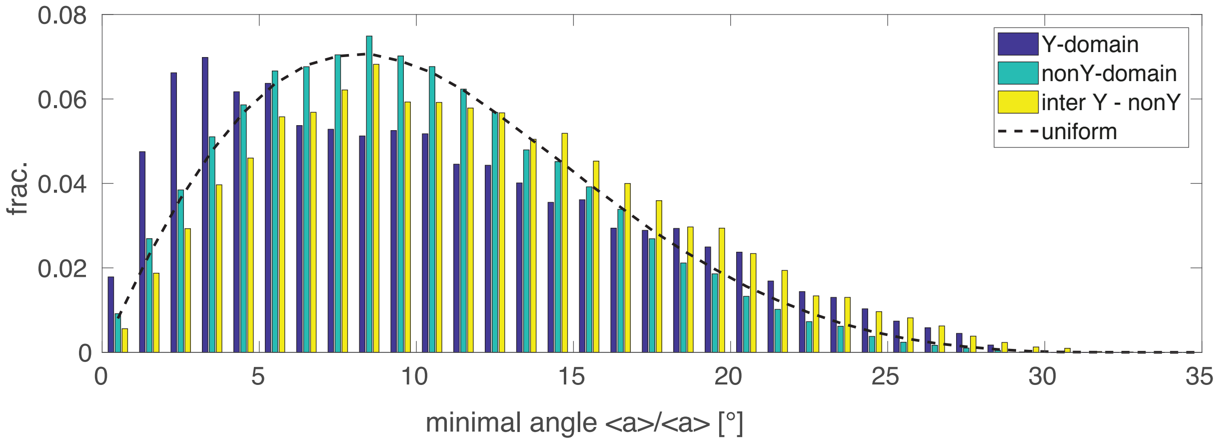

Solid Earth Discuss., doi:10.5194/se-2017-44, 2017
Manuscript under review for journal Solid Earth
Discussion started: 19 May 2017

Appendix Figure A3

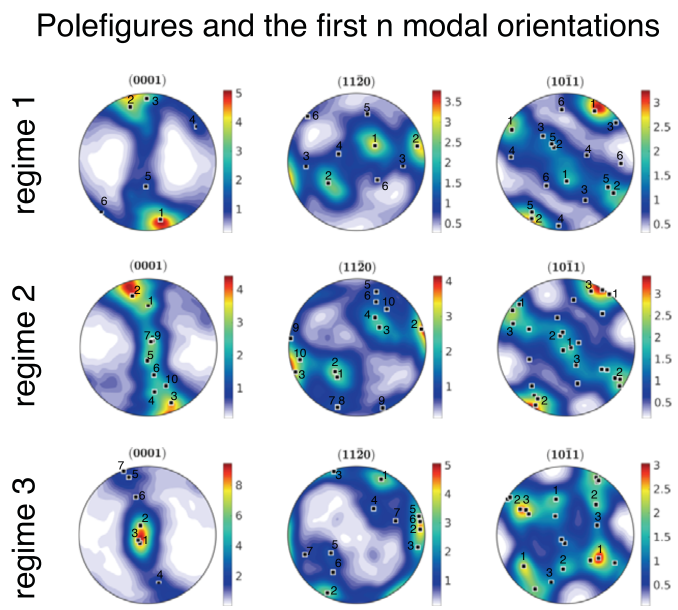

Solid Earth Discuss., doi:10.5194/se-2017-44, 2017
Manuscript under review for journal Solid Earth
Discussion started: 19 May 2017

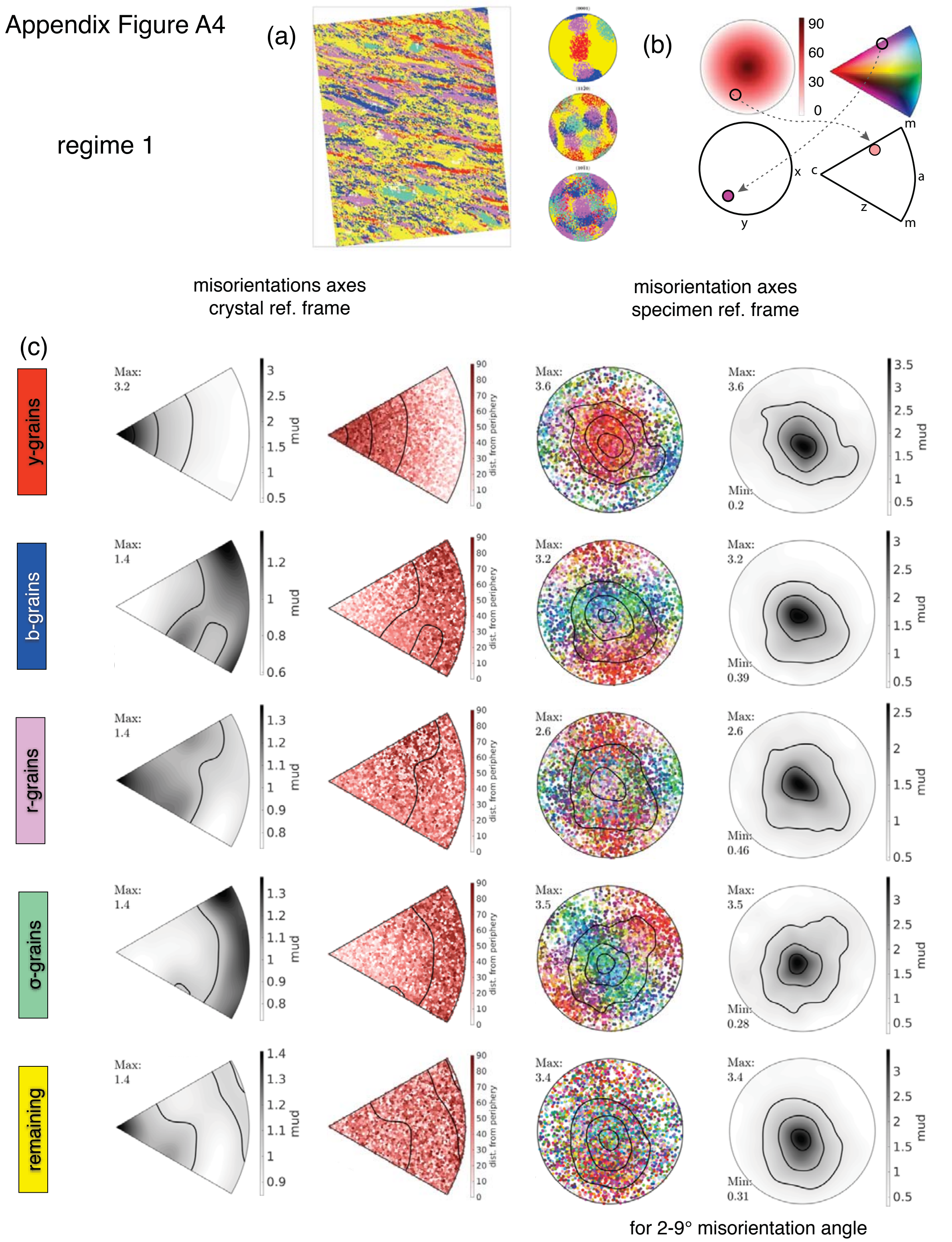

Solid Earth Discuss., doi:10.5194/se-2017-44, 2017
Manuscript under review for journal Solid Earth
Discussion started: 19 May 2017

Appendix Figure A4

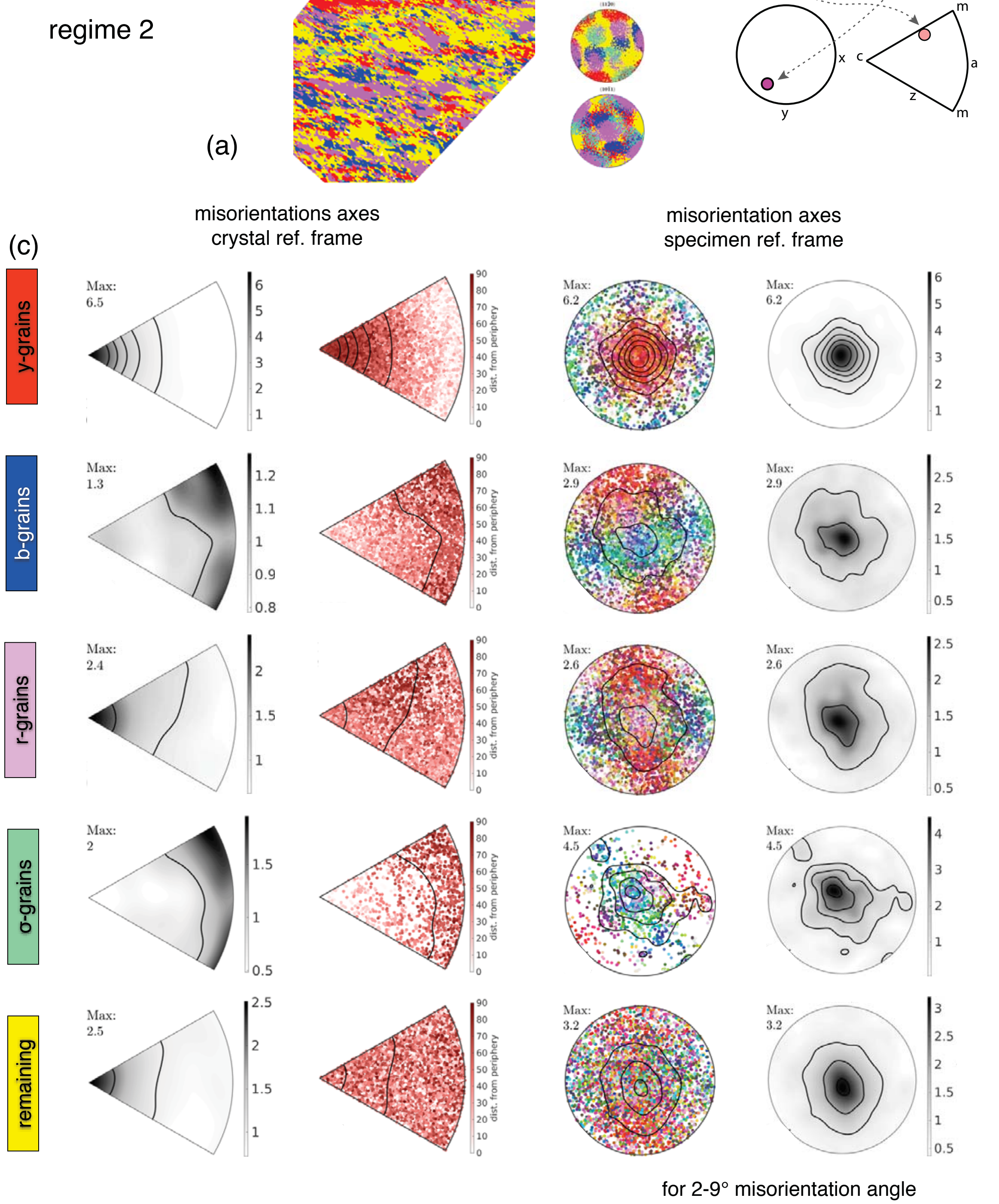

Solid Earth Discuss., doi:10.5194/se-2017-44, 2017
Manuscript under review for journal Solid Earth
Discussion started: 19 May 2017

Appendix Figure A4